Predicting Statistical Wave Physics in Complex Enclosures: A Stochastic Dyadic Green's Function Approach

Shen Lin, *Student Member, IEEE*, Sangrui Luo, *Student Member, IEEE*, Shukai Ma, *Student Member, IEEE*, Junda Feng, *Student Member, IEEE*, Yang Shao, *Member, IEEE*, Zachary B. Drikas, *Member, IEEE*, Bisrat D. Addissie, Steven M. Anlage, *Member, IEEE*, Thomas Antonsen, *Fellow, IEEE*, and Zhen Peng, *Senior Member, IEEE*

***Abstract*—This article presents a physics-oriented, mathematically tractable, statistical wave model for analyzing the wave physics of high-frequency reverberation in complex cavity environments. The key ingredient is a vector dyadic stochastic Green's function (SGF) method that is derived from the Wigner's random matrix theory and Berry's random wave hypothesis. The SGF statistically replicates multipath, ray-chaotic communication between vector sources and vectorial electromagnetic fields at displaced observation points using generic, macroscopic parameters of the cavity environment. The work establishes a physics-based modeling and simulation capability that predicts the probabilistic behavior of backdoor coupling to complex electronic enclosures. Experimental results are supplied to validate the proposed work.**

***Index Terms*—Chaos, electromagnetic coupling, Green function, intentional electromagnetic interference, statistical analysis.**

I. Introduction

THE study of electronics in strongly confined electromagnetic (EM) environments has long been a topic of interest in EM compatibility (EMC) and interference (EMI) communities [1], [2], [3], [4], [5], [6], [7], [8], [9], [10], [11], [12], [13]. One well-known example is the mode-stirred reverberation chamber, which has been utilized as a standard laboratory facility for EMC testing (emissions, immunity, shielding effectiveness, etc.) [14], [15], [16], [17], [18], and recently applied as an efficient emulator for wireless multipath fading scenarios [19], [20], [21], [22]. Another important application is the intentional EMI (IEMI) to electronics housed inside metallic enclosures (e.g., computer chassis, aircraft cabin) [23], [24], [25], [26], [27], [28], [29]. Radio-frequency (RF) power from external sources may penetrate into the target system through back-door channels, such as seams, apertures, and cooling vents [so-called "ports of entry (POEs)"]. The induced currents and voltages at the pins of internal electronics [so-called "ports of interference (POIs)"] may disrupt the normal functionality of circuits components, resulting in either a short/long-term electronic upset or permanent damage, subject to increased levels of pulsed energy. As electronics are increasingly densely packed, working at higher frequencies, and operating at lower voltages, they are more sensitive and vulnerable to IEMI effects.

It is recognized that wave propagation inside electrically large enclosures may undergo multiple reflection/scattering from boundaries and internal structures, thus leading to randomized phase, polarization, and direction of wave fields. In the short wavelength limit, the wave scattering process may exhibit chaotic ray trajectories, albeit underline wave equation is linear [30], [31], [32]. From the eigenmode perspective, the complex boundary of the enclosure can lead to high modal density and high modal overlap. Under high-frequency reverberation, the wave fields inside enclosures are very sensitive to the exact geometry of interior structures. Minor differences in the system configuration can result in significantly different EM field distributions inside the enclosure. Research regarding IEMI effects on electronic systems has shown large variations not only between designs but also between different serial numbers due to assembly methods, cable routing, and component variations [33].

Given the sensitive nature of electromagnetic wave physics to environmental details, it is crucial to develop stochastic models to account for the large variations in local field responses. In this regard, a stochastic Green's function (SGF) approach has been introduced in [34] as a model solution to the scalar wave equation in wave-chaotic environments. The SGF is based on the

Manuscript received 2 March 2022; revised 29 May 2022, 10 November 2022, and 20 December 2022; accepted 27 December 2022. The work was supported in part by the U.S. National Science Foundation (NSF) CAREER Award, #1750839, in part by the U.S. Office of Naval Research (ONR) Award #N00014-20-1-2835, and in part by the U.S. Defense Advanced Research Projects Agency (DARPA) Award #HR0011-21-2-00211. *(Corresponding author: Zhen Peng.)*

Shen Lin, Sangrui Luo, Junda Feng, Yang Shao, and Zhen Peng are with the Center for Computational Electromagnetics, Department of Electrical and Computer Engineering, The University of Illinois at Urbana-Champaign, Urbana, IL 61801 USA (e-mail: shenlin2@illinois.edu; sangrui2@illinois.edu; jundaf2@illinois.edu; yangshao@illinois.edu; zvpeng@illinois.edu).

Shukai Ma, Steven M. Anlage, and Thomas Antonsen are with the Electrical and Computer Engineering Department, and Institute for Research in Electronics and Applied Physics, University of Maryland, College Park, MD 20742 USA (e-mail: skma@umd.edu; anlage@umd.edu; antonsen@umd.edu).

Zachary B. Drikas and Bisrat D. Addissie are with the U.S. Naval Research Laboratory, Washington, DC 20375 USA (e-mail: zachary.drikas@nrl.navy.mil; bisrat.addissie@nrl.navy.mil).

Color versions of one or more figures in this article are available at https://doi.org/10.1109/TEMC.2023.3234912.

Digital Object Identifier 10.1109/TEMC.2023.3234912

physics of wave-chaotic systems [35], [36] and the mathematics of random matrix theory (RMT) [37], [38]. At its heart, the SGF makes use of a statistical representation of the eigenmodes and eigenfrequencies of an enclosed EM environment. The SGF has both a mean and fluctuating component, and thus, it separates the coherent and incoherent influences the currents in one element have on fields of another element. Moreover, the statistics of the SGF are determined by generic, macroscopic parameters of the cavity environment, including the operating frequency, cavity volume, loading, and wall losses. Thus, in applying the SGF details of the geometry that affect the precise spatial field distributions are dropped from the description, while the abovementioned generic parameters are retained in the formulation and allow for the calculation of the statistics of the field fluctuations.

In this article, we present a stochastic dyadic Green's function (DGF) approach as a means to relate the vector EM field to its vector source. The rationale behind this is that the variation and correlation of vectorial components are different at various locations, e.g., the center of the cavity, close to the wall, and close to the aperture. We have derived a mathematical framework accounting for all scenarios rigorously. Subsequently, we discuss the application of stochastic DGF (S-DGF) approach to three well-known problems of interest: 1) EM radiation and emission in complicated enclosures, 2) stochastic EM field coupling to conducting wires with loads, and 3) aperture coupling/excitation of large cavities from an external plane wave source. Finally, the proposed statistical models are validated in several experimental settings. These include the coupling of radiation to wires in a mode-stirred reverberation chamber and the excitation of an enclosure through apertures.

II. Methodology

A. Introduction to Scalar Stochastic Green's Function

Recently, a SGF approach [34] was introduced to model EM wave physics inside large enclosures using generic, macroscopic parameters of the cavity interior. The SGF can be considered as a theoretical extension of the random coupling model (RCM) [26], [39], [40] in which elements of the simulation domain are treated as "ports" in the wave-chaotic cavity environment. The basics of so-called wave chaos and RMT are discussed in [6], [7], [8], and [41]. Compared to previous works, the SGF combines coherent and incoherent propagation into a unified form, which includes universal statistical aspects predicted by the RMT as well as deterministic coupling characteristics.

Consider the second-order scalar wave equation inside a metallic cavity with distributed losses. The cavity wall will be treated as a perfect electric conductor (PEC) boundary condition. Inside the cavity, it is filled with a statistically homogeneous medium with permittivity ϵ and permeability μ. To account for the energy losses occurring inside the cavity, a uniform, finite conductivity σ of the medium is introduced. The Green's function for a source point at location $\mathbf{r}'$ satisfies

$$\left(\nabla^2 + \omega^2\mu\epsilon - j\omega\mu\sigma\right) G\left(\mathbf{r};\mathbf{r}'\right) = -\delta\left(\mathbf{r}-\mathbf{r}'\right). \tag{1}$$

If we introduce the following notations as in [42]: Wave number $k = \omega\sqrt{\mu\epsilon}$, and cavity quality factor $Q = \omega\epsilon/\sigma$, the Green's function can be constructed from the eigenfunction expansion using the cavity-mode theory [43], [44]

$$G\left(\mathbf{r},\mathbf{r}';k\right) = \sum_i \frac{\psi_i\left(\mathbf{r},k_i\right)\psi_i\left(\mathbf{r},'k_i\right)}{k^2 - k_i^2 - j\frac{k^2}{Q}} \tag{2}$$

where ψ_i and k_i are eigenfunctions (cavity eigenmodes) and eigenvalues (eigenfrequencies). It is noted that in principle we could introduce a statistical quality factor to account for the mode-dependent fluctuations in Q values. Our assumption is that we are considering losses that are not too localized in space. For example, the quality factor Q due to surface losses in a cavity with regular ray trajectories varies from mode to mode. However, if the ray trajectories are ergodic, as assumed here, each mode samples the losses equally and the modal fluctuations in quality factor are small [45], [46]. Even if losses are localized but there is a large number of localized loss regions, the fluctuations in quality factors are reduced [47].

As indicated by (2), the communication between source point $\mathbf{r}'$ and receiving point $\mathbf{r}$ is determined by a linear combination of cavity eigenmode contributions. Whereas (2) is in principle exact, it is impractical to compute these eigenfunctions and eigenvalues, due to the uncertainty and complexity of the environment.

In prior work [34], we prescribe substituting approximate, statistically defined eigenfunctions and eigenvalues. In particular, the eigenfunction statistics are derived from the Berry's random wave model [35] and eigenvalues statistics generated by the Wigner's random matrix theory [37]. The resulting Green's function, which is statistical in nature, is named the stochastic Green's function. The SGF may be considered an effective, probabilistic solution to wave propagation in wave-chaotic cavities, which statistically describes the coherent and incoherent components between a pair of source and receiving points. It can then be used to solve self-consistently for the wave propagation in the wave-chaotic media.

We remark that the statistics of the SGF do not depend on the exact geometry of the enclosure or the precise configuration of internal structures within the enclosure. Rather, they are determined by a few generic, macroscopic properties of the cavity environment, including the operating frequency, cavity volume, loading, and wall losses.

B. Development of Stochastic Dyadic Green's Function

In this work, we extend the scalar SGF to the S-DGF, which is particularly convenient for analyzing vectorial EM fields. Starting from the second-order vector wave equation inside a 3-D metallic cavity, the vector DGF for a source point at location $\mathbf{r}'$ satisfies

$$\nabla\times\nabla\times\overline{\overline{\mathbf{G}}} - \left(\omega^2\mu\epsilon - j\omega\mu\sigma\right)\overline{\overline{\mathbf{G}}}\left(\mathbf{r},\mathbf{r}'\right) = -\bar{\bar{\mathbf{I}}}\delta\left(\mathbf{r}-\mathbf{r}'\right). \tag{3}$$

The Green's function in the dyadic form can be constructed from the eigenfunction expansion

$$\overline{\overline{\mathbf{G}}}\left(\mathbf{r},\mathbf{r}'\right)=\sum_i \frac{\boldsymbol{\Psi}_i\left(\mathbf{r},k_i\right)\otimes\boldsymbol{\Psi}_i\left(\mathbf{r}',k_i\right)}{k^2-k_i^2-j\frac{k^2}{Q}} \tag{4}$$

where $\otimes$ indicates an outer product between two vectors. $\boldsymbol{\Psi}_i$ is the ith vector eigenfunction of the cavity with PEC boundary condition. The derivation of (4) is given in Appendix A.

In the following discussion, (4) will be reexpressed approximately by replacing the exact vector eigenmodes with approximate modes based on superpositions of random plane waves (RPW), and by replacing the exact eigenfrequency spectrum with one modeled by RMT. The goal is to arrive at a model DGF that replicates the statistical features of the exact DGF. The approximate modes and spectrum will thus be constrained by the properties of the actual cavity. The resulting statistical model does not predict precise values for a specific, well-defined geometry. Rather, it predicts the probability distribution function of cavity EM fields for an ensemble of statistically similar cavity environments.

Assuming both field and source points, $\mathbf{r}$, $\mathbf{r}'$ are far away from the cavity boundary, the eigenfunction $\boldsymbol{\Psi}_i$ is locally approximated by a superposition of many plane waves with uniformly distributed orientation and polarization

$$\boldsymbol{\Psi}_i\left(\mathbf{r},k_i\right)=\Psi_i^{\theta}\left(\mathbf{r},k_i\right)\hat{\theta}+\Psi_i^{\phi}\left(\mathbf{r},k_i\right)\hat{\phi} \tag{5}$$

with the vector components Ψ_i^{θ} and Ψ_i^{ϕ} expressed as

$$\Psi_i^{\theta}\left(\mathbf{r},k_i\right)\simeq\lim_{N\to\infty}\sum_{n=1}^{N}\left[a_n\cos\psi_n\cos\left(k_i\hat{\mathbf{e}}_n\cdot\mathbf{r}+\beta_n\right)\right] \tag{6}$$

$$\Psi_i^{\phi}\left(\mathbf{r},k_i\right)\simeq\lim_{N\to\infty}\sum_{n=1}^{N}\left[a_n\sin\psi_n\cos\left(k_i\hat{\mathbf{e}}_n\cdot\mathbf{r}+\beta_n\right)\right]. \tag{7}$$

The polarization angle ψ_n, direction $\hat{\mathbf{e}}_n$, and phase β_n are independent, uniform random variables. The amplitude a_n satisfies $\langle a_m a_n\rangle=\frac{2}{(NV)}\delta_{mn}$, in which V is the volume of the cavity.

The RPW hypothesis in (5) is argued on the basis that the waves, when thought of as rays, propagate through the enclosure chaotically and ergodically. This means that nearby rays diverge from each other exponentially, and eventually each ray visits everywhere at all angles. This requires that the internal surfaces of the enclosure not be shaped so as to create periodic ray trajectories which are stable in the sense that nearby trajectories do not diverge exponentially, e.g., a Fabrey–Perot resonator [48].

By converting the spherical coordinates to the Cartesian coordinates, we can rewrite (5) as

$$\boldsymbol{\Psi}_i\left(\mathbf{r},k_i\right)=\Psi_i^{x}\left(\mathbf{r}\right)\hat{\mathbf{x}}+\Psi_i^{y}\left(\mathbf{r}\right)\hat{\mathbf{y}}+\Psi_i^{z}\left(\mathbf{r}\right)\hat{\mathbf{z}} \tag{8}$$

where the vector components are

$$\Psi_i^{x}\left(\mathbf{r}\right)\simeq\lim_{N\to\infty}\sum_{n=1}^{N}[a_n(-\cos\psi_n\sin\phi_n- \sin\psi_n\cos\phi_n\cos\theta_n)\cos\left(k_i\hat{\mathbf{e}}_n\cdot\mathbf{r}+\beta_n\right)] \tag{9}$$

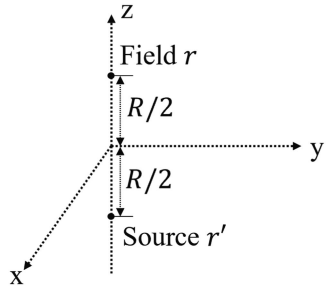

Fig. 1. Notation for the covariance derivation.

$$\Psi_i^{y}\left(\mathbf{r}\right)\simeq\lim_{N\to\infty}\sum_{n=1}^{N}[a_n(\cos\psi_n\cos\phi_n- \sin\psi_n\sin\phi_n\cos\theta_n)\cos\left(k_i\hat{\mathbf{e}}_n\cdot\mathbf{r}+\beta_n\right)] \tag{10}$$

$$\Psi_i^{z}\left(\mathbf{r}\right)\simeq\lim_{N\to\infty}\sum_{n=1}^{N}\left[a_n\sin\psi_n\sin\theta_n\cos\left(k_i\hat{\mathbf{e}}_n\cdot\mathbf{r}+\beta_n\right)\right]. \tag{11}$$

The central limit theorem implies, being the sum of contributions from a large number of RPWs, all Ψ_i^x, Ψ_i^y, and Ψ_i^z are zero mean Gaussian random variables. To derive their variances, we replace the sum over the plane wave contributions by a continuous average over all directions for the propagation vector and polarizations, i.e.,

$$\frac{1}{N}\sum_n[f]\approx\frac{1}{2\pi}\int_0^{2\pi}d\psi\frac{1}{4\pi}\int_0^{2\pi}d\phi\int_0^{\pi}d\theta\left[f\sin\theta\right]$$

where f represents a general function in terms of θ, ϕ, and ψ. As is shown in Appendix B, one can obtain the variances as

$$\mathcal{V}_{xx}=\left\langle\Psi_i^x\left(\mathbf{r}\right),\Psi_i^x\left(\mathbf{r}\right)\right\rangle=\frac{1}{3\,V} \tag{12}$$

$$\mathcal{V}_{yy}=\left\langle\Psi_i^y\left(\mathbf{r}\right),\Psi_i^y\left(\mathbf{r}\right)\right\rangle=\frac{1}{3\,V} \tag{13}$$

$$\mathcal{V}_{zz}=\left\langle\Psi_i^z\left(\mathbf{r}\right),\Psi_i^z\left(\mathbf{r}\right)\right\rangle=\frac{1}{3\,V} \tag{14}$$

$$\mathcal{V}_{xy}=\mathcal{V}_{xz}=\mathcal{V}_{yz}=0. \tag{15}$$

The next step is to derive the covariance between $\boldsymbol{\Psi}_i(\mathbf{r},k_i)$ and $\boldsymbol{\Psi}_i(\mathbf{r},'k_i)$. Without loss of generality, let $\mathbf{r}$ and $\mathbf{r}'$ located on the $\hat{\mathbf{z}}$-axis separating over a distance $R=|\mathbf{r}-\mathbf{r}'|$, as illustrated in Fig. 1. The covariance function between vectorial components can be derived as (the proofs are shown in Appendix C)

$$\mathcal{C}_{xx}(R)=\left\langle\Psi_i^x\left(\mathbf{r}\right),\Psi_i^x\left(\mathbf{r}'\right)\right\rangle=\frac{1}{3\,V}f_{\perp}\left(k_iR\right) \tag{16}$$

$$\mathcal{C}_{yy}(R)=\left\langle\Psi_i^y\left(\mathbf{r}\right),\Psi_i^y\left(\mathbf{r}'\right)\right\rangle=\frac{1}{3\,V}f_{\perp}\left(k_iR\right) \tag{17}$$

$$\mathcal{C}_{zz}(R)=\left\langle\Psi_i^z\left(\mathbf{r}\right),\Psi_i^z\left(\mathbf{r}'\right)\right\rangle=\frac{1}{3\,V}f_{//}\left(k_iR\right) \tag{18}$$

where $f_{\perp}(k_iR)$ and $f_{//}(k_iR)$ represent transversal and longitudinal correlation described by

$$f_{\perp}(k_iR) = \frac{3}{2}\left[\frac{\sin k_iR}{k_iR} - \frac{\sin k_iR - k_iR\cos k_iR}{(k_iR)^3}\right] \tag{19}$$

$$f_{//}(k_iR) = 3\frac{\sin(k_iR) - k_iR\cos(k_iR)}{(k_iR)^3}. \tag{20}$$

The results agree with the existing literature [49], [50].

We can then reveal the statistical property of eigenfunctions with correlated Gaussian random variables using the discrete Karhunen–Loeve expansion [51], [52]. The eigenfunctions are constructed by correlated Gaussian random variables w_i^x, w_i^y, w_i^z and $(w_i^x)'$, $(w_i^y)'$, $(w_i^z)'$, defined as

$$\boldsymbol{\Psi}_i(\mathbf{r}, k_i) \simeq w_i^x\hat{\mathbf{x}} + w_i^y\hat{\mathbf{y}} + w_i^z\hat{\mathbf{z}} \tag{21}$$

$$\boldsymbol{\Psi}_i(\mathbf{r},' k_i) \simeq (w_i^x)'\hat{\mathbf{x}} + (w_i^y)'\hat{\mathbf{y}} + (w_i^z)'\hat{\mathbf{z}} \tag{22}$$

where the covariance matrix of the six Gaussian random variables $[w_i^x, w_i^y, w_i^z, (w_i^x),' (w_i^y),' (w_i^z)']$ is given by

$$\begin{bmatrix} \mathcal{V}_{xx} & 0 & 0 & \mathcal{C}_{xx}(R) & 0 & 0 \\ 0 & \mathcal{V}_{yy} & 0 & 0 & \mathcal{C}_{yy}(R) & 0 \\ 0 & 0 & \mathcal{V}_{zz} & 0 & 0 & \mathcal{C}_{zz}(R) \\ \mathcal{C}_{xx}(R) & 0 & 0 & \mathcal{V}_{xx} & 0 & 0 \\ 0 & \mathcal{C}_{yy}(R) & 0 & 0 & \mathcal{V}_{yy} & 0 \\ 0 & 0 & \mathcal{C}_{zz}(R) & 0 & 0 & \mathcal{V}_{zz} \end{bmatrix}. \tag{23}$$

Accordingly, the outer product $\boldsymbol{\Psi}_i(\mathbf{r}, k_i) \otimes \boldsymbol{\Psi}_i(\mathbf{r}', k_i)$ can be written in a dyadic expression

$$\begin{aligned} \overline{\overline{\mathbf{D}}}(\mathbf{r}, \mathbf{r}'; k_i) = {} & w_i^x(w_i^x)'\hat{\mathbf{x}}\hat{\mathbf{x}} + w_i^x(w_i^y)'\hat{\mathbf{x}}\hat{\mathbf{y}} + w_i^x(w_i^z)'\hat{\mathbf{x}}\hat{\mathbf{z}} \\ & + w_i^y(w_i^x)'\hat{\mathbf{y}}\hat{\mathbf{x}} + w_i^y(w_i^y)'\hat{\mathbf{y}}\hat{\mathbf{y}} + w_i^y(w_i^z)'\hat{\mathbf{y}}\hat{\mathbf{z}} \\ & + w_i^z(w_i^x)'\hat{\mathbf{z}}\hat{\mathbf{x}} + w_i^z(w_i^y)'\hat{\mathbf{z}}\hat{\mathbf{y}} + w_i^z(w_i^z)'\hat{\mathbf{z}}\hat{\mathbf{z}}. \end{aligned} \tag{24}$$

It is easy to show that the mean value of above dyadic is

$$\left\langle \overline{\overline{\mathbf{D}}}(\mathbf{r}, \mathbf{r}'; k_i) \right\rangle = \mathcal{C}_{xx}(R)\hat{\mathbf{x}}\hat{\mathbf{x}} + \mathcal{C}_{yy}(R)\hat{\mathbf{y}}\hat{\mathbf{y}} + \mathcal{C}_{zz}(R)\hat{\mathbf{z}}\hat{\mathbf{z}}. \tag{25}$$

After incorporating the Berry's RPW hypothesis and statistical approximation of the eigenfunction outer product, (4) can be approximated by

$$\overline{\overline{\mathbf{G}}}_S(\mathbf{r}, \mathbf{r}'; k) \approx \sum_i \frac{\overline{\overline{\mathbf{D}}}(\mathbf{r}, \mathbf{r}'; k_i)}{k^2 - k_i^2 - j\frac{k^2}{Q}}. \tag{26}$$

Similar to the scalar SGF study, (26) can also be compared with the vector DGF in a homogeneous medium. We recall the well-known DGF formulation

$$\overline{\overline{\mathbf{G}}}_0(\mathbf{r}, \mathbf{r}'; k) = \left(\bar{\bar{\mathbf{I}}} + \frac{\nabla\nabla}{k^2}\right)\frac{e^{-jk|\mathbf{r}'-\mathbf{r}|}}{4\pi|\mathbf{r}'-\mathbf{r}|} \tag{27}$$

where $\bar{\bar{\mathbf{I}}}$ is the identity tensor. The explicit dyadic form of (27) can be written as

$$\begin{aligned} \overline{\overline{\mathbf{G}}}_0(\mathbf{r}, \mathbf{r}'; k) = \Bigg\{ & \left[\left(\frac{3}{k^2R^2} + \frac{3j}{kR} - 1\right)\hat{\mathbf{R}}\hat{\mathbf{R}} \right. \\ & \left. + \left(1 - \frac{j}{kR} - \frac{1}{k^2R^2}\right)\hat{\mathbf{I}}\right]\frac{e^{-jkR}}{4\pi R}\Bigg\}. \end{aligned} \tag{28}$$

Regarding the two points shown in Fig. 1, we have the real and imaginary parts

$$\begin{aligned} \mathrm{Re}\left[\overline{\overline{\mathbf{G}}}_0(\mathbf{r}, \mathbf{r}'; k)\right] = {} & \frac{k}{4\pi}\left[\left(\frac{2\cos kR + 2kR\sin kR}{k^3R^3}\right)\hat{\mathbf{z}}\hat{\mathbf{z}} \right. \\ & \left. + \left(\frac{\cos kR}{kR} - \frac{\cos kR + kR\sin kR}{k^3R^3}\right)(\hat{\mathbf{x}}\hat{\mathbf{x}} + \hat{\mathbf{y}}\hat{\mathbf{y}})\right] \end{aligned} \tag{29}$$

$$\begin{aligned} \mathrm{Im}\left[\overline{\overline{\mathbf{G}}}_0(\mathbf{r}, \mathbf{r}'; k)\right] = {} & \frac{k}{4\pi}\left[\left(\frac{2kR\cos kR - 2\sin kR}{k^3R^3}\right)\hat{\mathbf{z}}\hat{\mathbf{z}} \right. \\ & \left. - \left(\frac{\sin kR}{kR} - \frac{\sin kR - kR\cos kR}{k^3R^3}\right)(\hat{\mathbf{x}}\hat{\mathbf{x}} + \hat{\mathbf{y}}\hat{\mathbf{y}})\right]. \end{aligned} \tag{30}$$

In addition, by applying the Sokhotski–Plemelj theorem, the real part, $\mathrm{Re}\left[\overline{\overline{\mathbf{G}}}_0(\mathbf{r}, \mathbf{r}'; k)\right]$, can also be expressed as

$$\mathrm{Re}\left[\overline{\overline{\mathbf{G}}}_0(\mathbf{r}, \mathbf{r}'; k)\right] = -\frac{1}{\pi}\mathcal{P}\int \frac{dk_n^2}{k^2 - k_n^2}\mathrm{Im}\left[\overline{\overline{\mathbf{G}}}_0(\mathbf{r}, \mathbf{r}'; k_n)\right] \tag{31}$$

where $\mathcal{P}$ denotes the Cauchy principal value. Equation (31) gives rise to the Kramers–Kronig relation.

Next, by substituting (16)–(18) into (25), we can show that

$$\left\langle \overline{\overline{\mathbf{D}}}(\mathbf{r}, \mathbf{r}'; k_i) \right\rangle = -\frac{2\pi}{k_iV}\mathrm{Im}\left[\overline{\overline{\mathbf{G}}}_0(\mathbf{r}, \mathbf{r}'; k_i)\right]. \tag{32}$$

Starting from (26), we now take an average over the outer product of eigenfunctions. Since the eigenfunctions are orthogonal and the statistics of the eigenfunctions are taken to be independent of those of the eigenvalues in this process, we have

$$\left\langle \overline{\overline{\mathbf{G}}}_S(\mathbf{r}, \mathbf{r}'; k) \right\rangle = \sum_i \frac{\left\langle \overline{\overline{\mathbf{D}}}(\mathbf{r}, \mathbf{r}'; k_i) \right\rangle}{k^2 - k_i^2 - j\frac{k^2}{Q}} \tag{33}$$

$$= -\frac{1}{\pi}\sum_i \frac{2\pi^2}{k_iV}\frac{\mathrm{Im}[\overline{\overline{\mathbf{G}}}_0(\mathbf{r}, \mathbf{r}'; k_i)]}{k^2 - k_i^2 - j\frac{k^2}{Q}} \tag{34}$$

$$\simeq -\frac{1}{\pi}\sum_i \frac{\Delta(k_i^2)}{k^2 - k_i^2 - j\frac{k^2}{Q}}\mathrm{Im}\left[\overline{\overline{\mathbf{G}}}_0(\mathbf{r}, \mathbf{r}'; k_i)\right] \tag{35}$$

$$\approx -\frac{1}{\pi}\sum_i \frac{\Delta(k_i^2)}{\tilde{k}^2 - k_i^2}\mathrm{Im}\left[\overline{\overline{\mathbf{G}}}_0(\mathbf{r}, \mathbf{r}'; k_i)\right]. \tag{36}$$

In (35), we have introduced a function $\Delta(k_i^2) \simeq 2\pi^2/(k_iV)$, which can be understood as the approximate spacing between adjacent squared eigenvalues, $(k_{i+1}^2 - k_i^2)$. The physical justification goes as follows. For a 3-D EM cavity, the model density is given by the Weyl formula, $\rho(k) \sim (k^2\,V)/\pi^2$ [8]. Thereby, the spacing between adjacent eigenvalues can be expressed as $\Delta(k) = 1/\rho(k) \simeq \pi^2/(k^2\,V)$ and the spacing between squared eigenvalues is $\Delta(k^2) = 2k\Delta(k) \simeq 2\pi^2/(kV)$ [13].

In (36), a complex wavenumber $\tilde{k}$ is introduced as $\tilde{k} = k(1 - j/2Q)$. For electrically large, high-Q cavities, the $\tilde{k}^2$ can be

approximated as

$$\tilde{k}^2 = k^2\left(1-\frac{j}{Q}+\frac{1}{4Q^2}\right)\approx k^2\left(1-\frac{j}{Q}\right). \quad (37)$$

Comparing (36) and (31), the sum over eigenmodes can then be written as a frequency-domain integral on average. By using the Sokhotski–Plemelj theorem for the real line, the mean value of (36) approaches the deterministic, homogeneous dyadic Green function when $k/Q \ll 1$

$$\left\langle \overline{\overline{\mathbf{G}}}_S(\mathbf{r},\mathbf{r}';k)\right\rangle \approx \mathrm{Re}\left[\overline{\overline{\mathbf{G}}}_0(\mathbf{r},\mathbf{r}';k)\right]-j\mathrm{Im}\left[\overline{\overline{\mathbf{G}}}_0(\mathbf{r},\mathbf{r}';k)\right]. \quad (38)$$

The construction of the S-DGF is analogous to the RCM [8] and the scalar SGF [34]. We first separate the sum in (26) into two components. The first component consists of many terms in which the denominator has the property of $k_i^2 \not\approx k^2$, whereas the second component includes the terms with denominator $k_i^2 \approx k^2$. The mean value of the first component asymptotically reproduces the principal integral and, thereby can be expressed as Re $[\overline{\overline{\mathbf{G}}}_0(\mathbf{r},\mathbf{r}';k)]$. Moreover, the fluctuating contribution of S-DGF is dominated by the second component for which $k_i^2 \approx k^2$. Consequently, it suffices to construct the expression of S-DGF as

$$\overline{\overline{\mathbf{G}}}_{\mathrm{S}}(\mathbf{r},\mathbf{r}';k)\approx \mathrm{Re}\left[\overline{\overline{\mathbf{G}}}_0(\mathbf{r},\mathbf{r}';k)\right]+\sum_m \frac{\overline{\overline{\mathbf{D}}}(\mathbf{r},\mathbf{r}';k_m)}{\tilde{k}^2-k_m^2}. \quad (39)$$

When we apply the S-DGF to a point source electric current, the first part in (39) has the physical meaning of the reactive field that relates to the nonradiative, stored energy; whereas the second part represents the fluctuating radiative field.

Finally, we utilize the RMT to analyze the statistical property of cavity eigenvalues [34]. For problems satisfying the time-reversal symmetry, the Gaussian orthogonal ensemble (GOE) of random matrices is considered. After we calculate the eigenvalues $\tilde{\lambda}$ from the GOE random matrices, the statistical property of normalized eigenvalues is approximated by

$$\tilde{k}^2-k_m^2 \approx \left(\frac{k^2-k_m^2}{\bar{\Delta}}-j\frac{k^2}{\bar{\Delta}Q}\right)\bar{\Delta}\approx(\tilde{\lambda}_m-j\alpha)\bar{\Delta} \quad (40)$$

where the α is a macroscopic dimensionless loss-parameter defined by $\alpha = k^3\,V/(2\pi^2 Q)$, and the $\bar{\Delta}$ is the mean spacing between adjacent square eigenvalues when $k_m^2 \approx k^2$. According to the definition of $\Delta(k_m^2)$ function introduced following (36), we have $\bar{\Delta} = 2\pi^2/(kV)$. After incorporating the RMT approximation, the final expression of S-DGF is given by

$$\overline{\overline{\mathbf{G}}}_{\mathrm{S}}(\mathbf{r},\mathbf{r}';k)=\mathrm{Re}\left[\overline{\overline{\mathbf{G}}}_0(\mathbf{r},\mathbf{r}';k)\right]+\sum_m \frac{\overline{\overline{\mathbf{D}}}(\mathbf{r},\mathbf{r}';k_m)}{\tilde{\lambda}_m-j\alpha}\frac{kV}{2\pi^2}. \quad (41)$$

Equation (41) is a central result of our approach. It is an expression for the mean and fluctuating parts of the Green's function describing how a current source at point $\mathbf{r}$ creates a vector field at point $\mathbf{r}'$. Here it is assumed that the two points $\mathbf{r}$ and $\mathbf{r}'$ are both far from cavity boundaries and only the direct propagation of radiation from $\mathbf{r}$ to $\mathbf{r}'$ contributes to the mean part. The modifications to (41) when one or both of the points are near a boundary will be introduced in the next section. The fluctuating part of (41) is evaluated in two steps. First, one generates six zero mean Gaussian random variables from an ensemble with a covariance matrix given by (23). Then one inserts these random variables in (21) and (22). Finally, for each term in the sum evaluate the denominator using a numerically generated spectrum. It is through the covariance matrix and eigenvalue spacing distribution that information about the cavity under consideration is conveyed.

C. Analysis of Dipole Radiation Inside Enclosures

Equation (41) can be directly utilized to analyze electromagnetic radiation problems inside wave-chaotic environments. For example, we consider a small electric dipole of length l placed inside a 3-D metallic enclosure. The dipole is located at the origin with its wire directed along the $\hat{\mathbf{z}}$-axis. The current follows a triangular variation and the peak current at the center is denoted by I.

The radiated electric field can be expressed as

$$\mathbf{E}=j\omega\mu\int \overline{\overline{\mathbf{G}}}_{\mathrm{S}}(\mathbf{r},\mathbf{r}')\cdot\mathbf{J}(\mathbf{r}')\,d\mathbf{r}'=j\omega\mu\overline{\overline{\mathbf{G}}}_{\mathrm{S}}(\mathbf{r},\mathbf{r}')\cdot\hat{\mathbf{z}}\frac{Il}{2} \quad (42)$$

where the definition of S-DGF is given in (41).

When the field point is far away from the origin, the electric field is dominated by the incoherent (diffusive) propagation. Equation (42) simplifies to: $\mathbf{E}\approx j\omega\mu\overline{\mathbf{G}}_{\mathrm{S}}\frac{Il}{2}$, where the expression of $\overline{\mathbf{G}}_{\mathrm{S}}$ can be written as

$$\overline{\mathbf{G}}_{\mathrm{S}}=\sum_m \frac{w_m^x(w_m^z)'\hat{\mathbf{x}}+w_m^y(w_m^z)'\hat{\mathbf{y}}+w_m^z(w_m^z)'\hat{\mathbf{z}}}{\tilde{\lambda}_m-j\alpha}\frac{kV}{2\pi^2} \quad (43)$$

where w_m^x, w_m^y, w_m^z, and $(w_m^z)'$ are independent, zero mean Gaussian random variables.

Namely, the radiated electric field $\mathbf{E}$ consists of three diffuse scalar components

$$\mathrm{E}_x = j\omega\mu\frac{Il}{2}\frac{kV}{2\pi^2}\sum_m\frac{w_m^x(w_m^z)'}{\tilde{\lambda}_m-j\alpha}=j\omega\mu\frac{Il}{2}\frac{kV}{2\pi^2}g_{xz} \quad (44)$$

$$\mathrm{E}_y = j\omega\mu\frac{Il}{2}\frac{kV}{2\pi^2}\sum_m\frac{w_m^y(w_m^z)'}{\tilde{\lambda}_m-j\alpha}=j\omega\mu\frac{Il}{2}\frac{kV}{2\pi^2}g_{yz} \quad (45)$$

$$\mathrm{E}_z = j\omega\mu\frac{Il}{2}\frac{kV}{2\pi^2}\sum_m\frac{w_m^z(w_m^z)'}{\tilde{\lambda}_m-j\alpha}=j\omega\mu\frac{Il}{2}\frac{kV}{2\pi^2}g_{zz} \quad (46)$$

where we have introduced three parameters g_{xz}, g_{yz}, and g_{zz} to simplify the expression. Those parameters depend on Gaussian random variables w_m^x, w_m^y, w_m^z, RMT-based calculation of eigenvalues $\tilde{\lambda}_m$, and the cavity loss-parameter α. Since the Gaussian random variables are uncorrelated, the mean value of E_x, E_y, or E_z is zero. Often at times, one may also be interested in the mean of the squared electric field amplitude, as it is related to the energy density inside the cavity. To derive it, we first need to calculate the variance of g_{xz}, g_{yz}, and g_{zz} in (44)–(46).

Appendix D provides the detailed derivation. The results show that the variance is: $\mathrm{Var}(g_{xz}) = \mathrm{Var}(g_{yz}) = \mathrm{Var}(g_{zz}) = \pi/(9\,V^2\alpha)$. As a result, the mean of the squared amplitude of scalar components is derived as

$$\left\langle|\mathrm{E}_x|^2\right\rangle=\left\langle|\mathrm{E}_y|^2\right\rangle=\left\langle|\mathrm{E}_z|^2\right\rangle=\frac{\omega^2\mu^2}{72\pi}\frac{Q}{kV}(Il)^2. \quad (47)$$

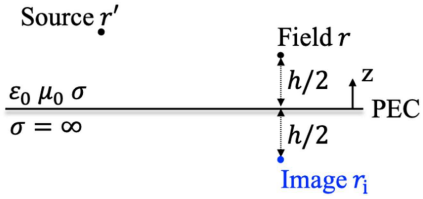

Fig. 2. Illustration of wave field close to cavity boundary.

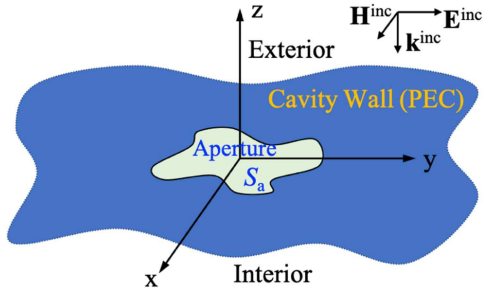

Fig. 3. Illustration for the aperture coupling problem.

Therefore, the mean value of the squared amplitude of vector electric field $\mathbf{E}$ reads

$$\left\langle |\mathbf{E}|^2 \right\rangle = \left\langle |\mathrm{E}_x|^2 \right\rangle + \left\langle |\mathrm{E}_y|^2 \right\rangle + \left\langle |\mathrm{E}_z|^2 \right\rangle = \frac{\omega^2 \mu^2}{24\pi} \frac{Q\,(\mathrm{I}l)^2}{kV}. \tag{48}$$

In a reverberation chamber setting, the result of (48) is related to the square of the chamber constant. Equation (48) will be used in Section III-B to generate a reverberation chamber environment.

D. Analysis of Wave Field Close to Planar Boundary

We note that in the derivation of S-DGF method, both source and receiving points are assumed to be away from cavity walls. Cavity eigenfunctions can, thereby be locally approximated by an isotropic, random superposition of plane waves. It is clearly not the case in the evaluation of wave fields close to cavity boundaries. Due to the presence of close-by walls, the statistical properties of S-DGF are different from the uniform, isotropic case. In particular, when the field point is located at the highly conducting wall, the EM boundary condition needs to be satisfied exactly.

For the purpose of illustration, we consider the case of source electric current located at $\mathbf{r}'$ radiating electric field inside a metallic cavity. The receiving field point at $\mathbf{r}$ is close to a planar cavity wall on the xy plane, as shown in Fig. 2. To incorporate the reflected field from the cavity wall, the RPW approximation of eigenfunctions in (8) is modified as

$$\begin{aligned} \boldsymbol{\Psi}_i^{\mathrm{e}}(\mathbf{r}) \simeq\ & \tilde{\Psi}_i^x(\mathbf{r})\,\hat{\mathbf{x}} + \tilde{\Psi}_i^y(\mathbf{r})\,\hat{\mathbf{y}} + \tilde{\Psi}_i^z(\mathbf{r})\,\hat{\mathbf{z}} \\ & - \tilde{\Psi}_i^x(\mathbf{r}_{\mathrm{i}})\,\hat{\mathbf{x}} - \tilde{\Psi}_i^y(\mathbf{r}_{\mathrm{i}})\,\hat{\mathbf{y}} + \tilde{\Psi}_i^z(\mathbf{r}_{\mathrm{i}})\,\hat{\mathbf{z}} \end{aligned} \tag{49}$$

where $\mathbf{r}_{\mathrm{i}} (= x\hat{\mathbf{x}} + y\hat{\mathbf{y}} - z\hat{\mathbf{z}})$ denotes the image position of $\mathbf{r} (= x\hat{\mathbf{x}} + y\hat{\mathbf{y}} + z\hat{\mathbf{z}})$. Since $\tilde{\Psi}$ only consists of the plane waves propagating toward the boundary, $\left\langle \tilde{\Psi}_i^*, \tilde{\Psi}_i^* \right\rangle = \langle \Psi_i^*, \Psi_i^* \rangle / 2$.

The variances of vector components in $\boldsymbol{\Psi}_i^{\mathrm{e}}$ are derived in Appendix E. The results are as follows:

$$\mathcal{V}_{xx} = \left\langle \hat{\mathbf{x}} \cdot \boldsymbol{\Psi}_i^{\mathrm{e}}(\mathbf{r}), \hat{\mathbf{x}} \cdot \boldsymbol{\Psi}_i^{\mathrm{e}}(\mathbf{r}) \right\rangle = \frac{1}{3V}\left[1 - f_{\perp}(k_i h)\right] \tag{50}$$

$$\mathcal{V}_{yy} = \left\langle \hat{\mathbf{y}} \cdot \boldsymbol{\Psi}_i^{\mathrm{e}}(\mathbf{r}), \hat{\mathbf{y}} \cdot \boldsymbol{\Psi}_i^{\mathrm{e}}(\mathbf{r}) \right\rangle = \frac{1}{3V}\left[1 - f_{\perp}(k_i h)\right] \tag{51}$$

$$\mathcal{V}_{zz} = \left\langle \hat{\mathbf{z}} \cdot \boldsymbol{\Psi}_i^{\mathrm{e}}(\mathbf{r}), \hat{\mathbf{z}} \cdot \boldsymbol{\Psi}_i^{\mathrm{e}}(\mathbf{r}) \right\rangle = \frac{1}{3V}\left[1 + f_{//}(k_i h)\right]. \tag{52}$$

The variations in the transverse and longitudinal components act differently, as indicated in the expression. When the observation point $\mathbf{r}$ is far away from the boundary, i.e., $k_i h \gg 1$, we have $f_{\perp}(k_i h) \approx 0$ and $f_{//}(k_i h) \approx 0$. The variations in (50)–(52) will reduce to the uniform case in (12)–(14). At the wall boundary $z = 0$, i.e., $k_i h = 0$, we have $f_{\perp}(k_i h) \approx 1$ and $f_{//}(k_i h) \approx 1$, thereby

$$\mathcal{V}_{xx} = \mathcal{V}_{yy} = 0 \tag{53}$$

$$\mathcal{V}_{zz} = \frac{2}{3V} \tag{54}$$

where the tangential components are zero and the normal component is doubled, thereby the boundary condition of the eigenfunction is enforced.

To simplify the expression of the resulting vector SGF, we may rewrite (49) as

$$\boldsymbol{\Psi}_i^{\mathrm{e}}(\mathbf{r}) = \tilde{\boldsymbol{\Psi}}_i^{\mathrm{e}}(\mathbf{r}) - \tilde{\boldsymbol{\Psi}}_i^{\mathrm{e}}(\mathbf{r}_{\mathrm{i}}) + 2\hat{\mathbf{z}}\hat{\mathbf{z}} \cdot \tilde{\boldsymbol{\Psi}}_i^{\mathrm{e}}(\mathbf{r}_{\mathrm{i}}). \tag{55}$$

By following a similar procedure in Section II-B to derive the eigenfunction tensor product, $\boldsymbol{\Psi}_i^{\mathrm{e}}(\mathbf{r}) \otimes \boldsymbol{\Psi}_i(\mathbf{r}')$, we can obtain the vector dyadic SGF for the boundary electric field

$$\overline{\overline{\mathbf{G}}}_S^{\mathrm{e,j}}(\mathbf{r}, \mathbf{r}') = \overline{\overline{\mathbf{G}}}_S(\mathbf{r}, \mathbf{r}') - \overline{\overline{\mathbf{G}}}_S(\mathbf{r}_{\mathrm{i}}, \mathbf{r}') + 2\hat{\mathbf{z}}\hat{\mathbf{z}} \cdot \overline{\overline{\mathbf{G}}}_S(\mathbf{r}_{\mathrm{i}}, \mathbf{r}'). \tag{56}$$

The expression has an analogy with the well-known half-space electric DGF of the first kind [53].

E. Analysis of Cavity Aperture Excitation

In many practical electronic systems, the enclosure may be open to the outside with multiple apertures in the cavity wall. Given the incident external RF radiation, the size and shape of the aperture determine the amount of EM power coupled into the cavity. Therefore, it is important to quantitatively study the site-specific aperture excitation and coupling [23], [54], [55], [56], [57], [58].

Consider a cavity wall with an irregular aperture sitting in the xy plane, as illustrated in Fig. 3. The aperture is illuminated by an EM plane wave due to external RF sources. We start by introducing an artificial surface S_a over the aperture opening. The computational domain can then be decomposed into the interior confined cavity subregion and exterior host body subregion. Naturally, the exterior traveling wave physics and interior cavity resonance physics can then be separated.

Based on the equivalence principle, one can obtain an equivalent exterior problem by filling the interior subregion with a PEC. The exterior subregion is then formulated by a surface integral

equation (SIE), whose unknowns involve the magnetic current $\mathbf{M}^{+}=\mathbf{E}\times\hat{\mathbf{z}}$ at the aperture [54]. At the aperture surface, we have the magnetic field relation

$$\mathbf{H}_t^{+}(\mathbf{r})=2\mathbf{H}_t^{\mathrm{inc}}(\mathbf{r})+\mathbf{H}_t^{\mathrm{R},+}(\mathbf{r})\ \text{ on } S_a. \tag{57}$$

The $\mathbf{H}_t^{+}$ represents the tangential components of the total magnetic field. The $\mathbf{H}_t^{\mathrm{inc}}$ denotes the tangential components of the incident magnetic field. The $\mathbf{H}_t^{\mathrm{R},+}$ represents the tangential components of radiated magnetic field by the surface magnetic current $\mathbf{M}^{+}$. Assuming a locally quasi-planar cavity wall at the aperture location, we have

$$\mathbf{H}_t^{\mathrm{R},+}(\mathbf{r})=2\frac{jk_0}{\eta}\pi_\tau\left(\iint_{S_a}\overline{\overline{\mathbf{G}}}_0(\mathbf{r},\mathbf{r}')\cdot\mathbf{M}^{+}(\mathbf{r}')\,dS'\right) \tag{58}$$

where the $\eta=\sqrt{\frac{\mu}{\epsilon}}$ is the wave impedance, the $\pi_\tau(\bullet)$ is a tangential trace operator defined by: $\pi_\tau(\mathbf{u}):=\hat{\mathbf{n}}\times(\mathbf{u}\times\hat{\mathbf{n}})|_{S_a}$. Here the surface normal $\hat{\mathbf{n}}=\hat{\mathbf{z}}$ for the exterior subregion.

An equivalent problem can be obtained for the interior cavity subregion with the aperture covered by an electric conductor. To formulate the aperture SIE of the interior subregion, we first introduce the electric S-DGF of the second kind starting from the eigenfunction expansion

$$\overline{\overline{\mathbf{G}}}_S^{\mathrm{h,m}}(\mathbf{r},\mathbf{r}')=\sum_i\frac{\boldsymbol{\Psi}_i^{\mathrm{h}}(\mathbf{r},k_i)\otimes\boldsymbol{\Psi}_i^{\mathrm{m}}(\mathbf{r}',k_i)}{k^2-k_i^2-j\frac{k^2}{Q}}. \tag{59}$$

As comparable to (49), the RPW approximation of the magnetic field eigenfunction $\boldsymbol{\Psi}_i^{\mathrm{h}}(\mathbf{r})$ can be expressed as

$$\begin{aligned}\boldsymbol{\Psi}_i^{\mathrm{h}}(\mathbf{r})\simeq{}&\tilde{\Psi}_i^{x}(\mathbf{r})\,\hat{\mathbf{x}}+\tilde{\Psi}_i^{y}(\mathbf{r})\,\hat{\mathbf{y}}+\tilde{\Psi}_i^{z}(\mathbf{r})\,\hat{\mathbf{z}}\\&+\tilde{\Psi}_i^{x}(\mathbf{r}_{\mathrm{i}})\,\hat{\mathbf{x}}+\tilde{\Psi}_i^{y}(\mathbf{r}_{\mathrm{i}})\,\hat{\mathbf{y}}-\tilde{\Psi}_i^{z}(\mathbf{r}_{\mathrm{i}})\,\hat{\mathbf{z}}.\end{aligned} \tag{60}$$

A similar expression of the RPW model is used for the source eigenfunction $\boldsymbol{\Psi}_i^{\mathrm{m}}(\mathbf{r}')$

$$\begin{aligned}\boldsymbol{\Psi}_i^{\mathrm{m}}(\mathbf{r}')\simeq{}&\tilde{\Psi}_i^{x}(\mathbf{r}')\,\hat{\mathbf{x}}+\tilde{\Psi}_i^{y}(\mathbf{r}')\,\hat{\mathbf{y}}+\tilde{\Psi}_i^{z}(\mathbf{r}')\,\hat{\mathbf{z}}\\&+\tilde{\Psi}_i^{x}(\mathbf{r}_{\mathrm{i}}')\,\hat{\mathbf{x}}+\tilde{\Psi}_i^{y}(\mathbf{r}_{\mathrm{i}}')\,\hat{\mathbf{y}}-\tilde{\Psi}_i^{z}(\mathbf{r}_{\mathrm{i}}')\,\hat{\mathbf{z}}.\end{aligned} \tag{61}$$

The aperture SIE for the interior subregion in terms of magnetic field is given by

$$\mathbf{H}_t^{\mathrm{R},-}(\mathbf{r})=\frac{jk_0}{\eta}\pi_\tau\left(\iint_{S_a}\overline{\overline{\mathbf{G}}}_S^{\mathrm{h,m}}(\mathbf{r},\mathbf{r}')\cdot\mathbf{M}^{-}(\mathbf{r}')\,dS'\right) \tag{62}$$

where the equivalent magnetic current $\mathbf{M}^{-}=\mathbf{E}\times(-\hat{\mathbf{z}})=-\mathbf{M}^{+}$ enforces the continuity of tangential electric field at the aperture. It is noted that the radiated magnetic field, $\mathbf{H}_t^{\mathrm{R},-}(\mathbf{r})$, is the same as the total magnetic field $\mathbf{H}_t^{-}(\mathbf{r})$ as there is no incident field inside the cavity.

Finally, by applying the boundary condition at the aperture, i.e., the continuity of magnetic fields for exterior and interior subregions, $\mathbf{H}_t^{+}(\mathbf{r})=\mathbf{H}_t^{-}(\mathbf{r})$, we have

$$-\mathbf{H}^{\mathrm{R},+}(\mathbf{r})+\mathbf{H}^{\mathrm{R},-}(\mathbf{r})=2\mathbf{H}_t^{\mathrm{inc}}(\mathbf{r})\ \text{ on } S_a. \tag{63}$$

Through interface condition and the Galerkin testing method [59], the surface IEs in (58), (62), and (63) can be cast in a matrix equation of the following form:

$$[\mathbf{Y}_0^{\mathrm{h,m}}+\mathbf{Y}_S^{\mathrm{h,m}}]\overline{\mathbf{M}}=\overline{\mathbf{H}}^{\mathrm{inc}} \tag{64}$$

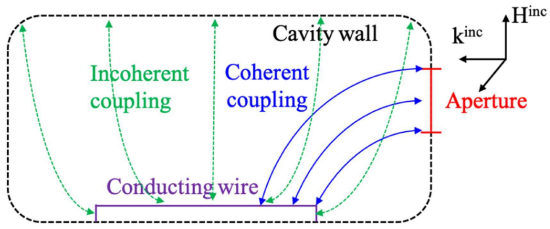

Fig. 4. Schematic diagram of conducting wire problem.

where the $\overline{\mathbf{H}}^{\mathrm{inc}}$ represents the excitation vector. The $\mathbf{Y}_0^{\mathrm{h,m}}$ is the aperture admittance matrix for the exterior region in terms of free-space DGF, whereas the $\mathbf{Y}_S^{\mathrm{h,m}}$ is the aperture admittance matrix for the interior cavity region. The detailed expression of (64) is given in Appendix F. The solution of aperture currents can then be used to analyze the statistics of transmitted power into the enclosure as well as the statistical shielding effectiveness. The variability is due to only approximately known information of the interior cavity being used to construct the S-DGF model.

F. Stochastic Field Coupling to Conducting Wires

Wires and cables are routinely used in electronic systems to interconnect antennas, printed circuit boards, and electronic components. They often introduce additional coupling paths from external IEMI sources to sensitive circuitry inside computer enclosures. Thereby, it is important to study the mechanism of wire coupling and interference from the external RF sources. In general, the induced current and voltage on the wire/cable depend on the self-capacitance, self-inductance, length and radius of the wire, load impedances at the terminal, and statistical EM fields inside the electronic enclosure [60], [61], [62], [63], [64], [65].

A generic problem statement is given in Fig. 4. A U-shaped thin conducting wire is placed parallel to the cavity wall with both ends terminated with linear loads. Assuming the wire radius is much smaller than the wavelength, we can neglect the transverse component of the current inside the wire. Namely, the electric current only has a longitudinal component that is uniformly distributed over the periphery of the wire. The induced current $\mathbf{J}_l$ along the wire and voltages at the port, due to an incident EM wave, can then be calculated by an electric field integral equation (EFIE) [66].

With the Galerkin method and appropriate basis along with the testing functions, the problem of stochastic EM fields coupling from the aperture to the conducting wire can be recast in a matrix equation of the following compact form:

$$\begin{bmatrix}\mathbf{Y}_0^{\mathrm{h,m}}+\mathbf{Y}_S^{\mathrm{h,m}} & \mathbf{C}_S^{\mathrm{h,j}}\\ \mathbf{C}_S^{\mathrm{e,m}} & \mathbf{Z}_S^{\mathrm{e,j}}\end{bmatrix}\begin{bmatrix}\overline{\mathbf{M}}_a\\ \overline{\mathbf{J}}_l\end{bmatrix}=\begin{bmatrix}\overline{\mathbf{H}}^{\mathrm{inc}}\\ 0\end{bmatrix} \tag{65}$$

where $\overline{\mathbf{M}}_a$ and $\overline{\mathbf{J}}_l$ are solution vectors for magnetic current at the aperture and electric current on the conducting wire. Comparing with (64), we have included the stochastic IE matrix $\mathbf{Z}_S^{\mathrm{e,j}}$ accounting for the EFIE of conducting wire, in which triangular functions are used as basis and testing functions. Note that the

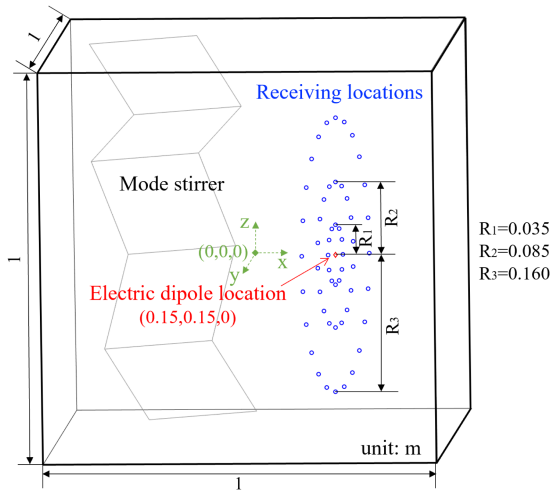

Fig. 5. Illustration of the numerical experiment for the dipole radiation problem.

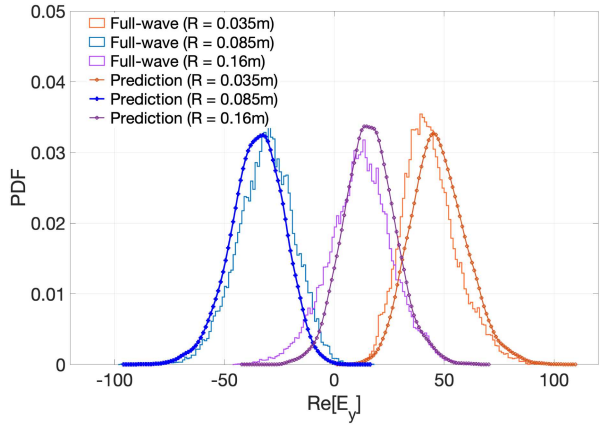

Fig. 6. PDFs of $\mathrm{Re}[\mathrm{E}_y]$ comparing full-wave simulations and statistical predictions.

coupling matrices, $\mathbf{C}_S^{\mathrm{h,j}}$ and $\mathbf{C}_S^{\mathrm{e,m}}$ between aperture and wire are also generated by the stochastic IE operator with the S-DGF as the kernel.

By solving (65) with different S-DGF IE matrices in the statistical ensemble, one can predict the statistics of induced voltages/currents at the wire ports due to coupled EM fields inside the enclosure, as a function of frequency and incident angle of external IEMI sources.

We remark that as the Green's function and integral equation methods are used to model the metal wire, both transmission line physics and high-frequency field coupling are modeled correctly. Furthermore, the proposed S-DGF rigorously integrates both the coherent propagation from apertures to conducting wires, and incoherent diffuse coupling due to multiple rays bounced from the cavity wall. Therefore, the statistical prediction of conducting wire pickup incorporates the relative location and orientation between apertures and wires, which is another unique aspect of the proposed work.

III. Validation and Verification

A. Electromagnetic Radiation in Wave-Chaotic Enclosures

The first numerical study concerns an EM radiation problem with a small electric dipole of length l inside a 3-D metallic enclosure. The goal is to validate the statistics of radiated electric field predicted by the S-DGF in (41) with full-wave numerical simulations. The results will be useful to assess fundamental EM radiation properties inside wave-chaotic enclosures.

The design of the numerical experiment is illustrated in Fig. 5. The dimension of the cavity is $[-0.5\ \mathrm{m}, 0.5\ \mathrm{m}]$:$[-0.5\ \mathrm{m}, 0.5\ \mathrm{m}]$:$[-0.5\ \mathrm{m}, 0.5\ \mathrm{m}]$ in length, width, and height. The cavity wall is treated as the PEC boundary condition. The cavity volume is filled with a lossy dielectric material with a dielectric constant of 1 and a loss tangent of 0.00194 at 2.475 GHz. Together with the cavity volume $1\ \mathrm{m}^3$, we can obtain the cavity quality factor $Q = 515.625$ and the cavity loss parameter $\alpha = 13.7$. A small electric dipole of length $l = 4\,\mathrm{mm}$ directed along with $\hat{\mathbf{y}}$-axis is placed at $[0.15\ \mathrm{m}, 0.15\ \mathrm{m}, 0\ \mathrm{m}]$. The current follows a triangular variation and the peak current at the center is denoted by $\mathrm{I} = 1\ \mathrm{A}$. Finally, to generate a configuration ensemble in the full-wave simulation, we have included an irregular Z-folded stirrer consisting of five 0.3 by 0.3- m metallic plates that are arranged in different folding angles. The center of the stirrer is located at $x = -0.25\,\mathrm{m}$ and $y = -0.25\,\mathrm{m}$.

On the statistical prediction using the S-DGF method, we can express the radiated electric field as

$$\mathbf{E} = j\omega\mu \int \overline{\overline{\mathbf{G}}}_{\mathrm{S}}(\mathbf{r}, \mathbf{r}') \cdot \mathbf{J}(\mathbf{r}')\, d\mathbf{r}' = j\omega\mu \overline{\overline{\mathbf{G}}}_{\mathrm{S}}(\mathbf{r}, \mathbf{r}') \cdot \hat{\mathbf{y}} \frac{Il}{2}. \tag{66}$$

To assess the statistics of radiated E-field as a function of distance to the dipole, we consider a number of probe locations inside the same xz-plane as the dipole. The y component of the electric field at a probe location can be expressed as

$$\mathrm{E}_y = \frac{k\omega\mu Il V}{4\pi} \left[\frac{j}{2V} \left(\frac{\cos kR}{kR} - \frac{\cos kR + kR \sin kR}{k^3 R^3} \right) + \frac{j}{\pi} \sum_m \frac{\omega_m^y (\omega_m^y)'}{\tilde{\lambda}_m - j\alpha} \right]. \tag{67}$$

It is noted that due to the coherent coupling between the source and receiving points, ω_m^y and $(\omega_m^y)'$ are correlated Gaussian random variables, constructed by the covariance matrix in (23).

Regarding the full-wave simulation, we have used a commercial software (CST) to simulate the same EM radiation problem. In the simulation setup, the mode stirrer is rotated through 12 positions over 360 degrees. At each stirrer position, we collect electric field samples at the xz plane of dipole location from 2.45 to 2.5-GHz with 0.25-MHz increment. Around 36, 54, 72 k samples of electric fields are collected at circles of radius $R_1 = 0.035\ \mathrm{m}$, $R_2 = 0.085\ \mathrm{m}$, $R_3 = 0.16\ \mathrm{m}$, respectively.

The probability density functions (PDFs) obtained from full-wave simulation and the S-DGF prediction are plotted for $\mathrm{Re}[\mathrm{E}_y]$, $\mathrm{Im}[\mathrm{E}_y]$, and amplitude $|\mathrm{E}_y|$ in Figs. 6–8. The mean

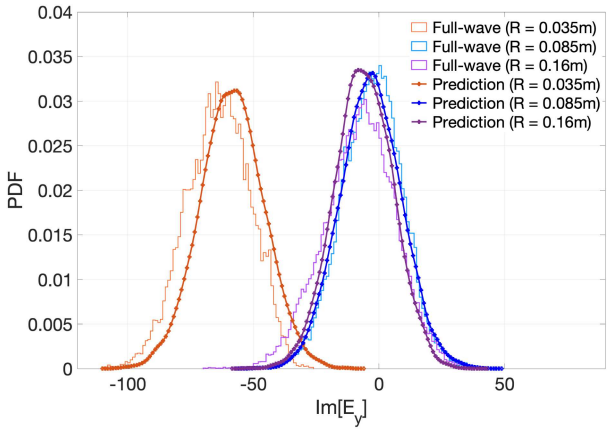

Fig. 7. PDFs of $\mathrm{Im}[\mathrm{E}_y]$ comparing full-wave simulations and statistical predictions.

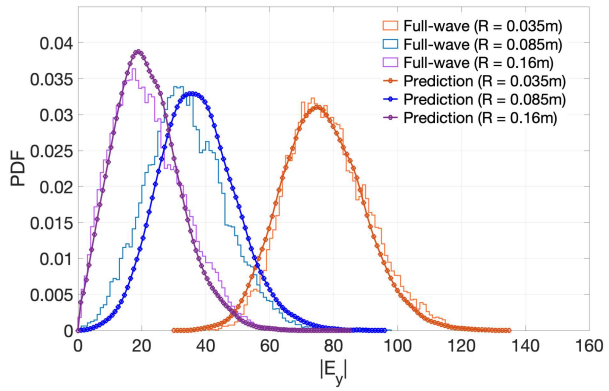

Fig. 8. PDFs of E_y amplitude comparing full-wave simulations and statistical predictions.

TABLE I
MEAN VALUES OF $\mathrm{Re}[\mathrm{E}_y]$ AND $\mathrm{Im}[\mathrm{E}_y]$

R	CST		Proposed work	
	$\mathrm{Re}[\mathrm{E}_y]$	$\mathrm{Im}[\mathrm{E}_y]$	$\mathrm{Re}[\mathrm{E}_y]$	$\mathrm{Im}[\mathrm{E}_y]$
0.035m	43.525	-64.014	47.580	-58.492
0.085m	-31.265	-2.745	-35.104	-3.257
0.16m	11.888	-7.727	16.127	-6.149

values of the data are given in Table I. We observe that, as the distance between the dipole location and receiving point decreases, there is an increase in the coherent coupling component, which results in a larger mean value. The results show generally good agreement between the first-principles simulation and the statistical prediction.

B. stochastic Field Coupling to a Conducting Wire

In the literature, the stochastic field-to-wire coupling has been studied theoretically and experimentally in reverberation chambers. For this validation, the mode-stirred chamber described in [67] is used. The dimensions of the chamber are $7.9 \times 6.5 \times 3.5\,\mathrm{m}$. The U-shaped conducting wire has a length $1.1\ \mathrm{m}$ and a 4-mm^2 cross-section. The distance between the parallel segment to the chamber wall is 32 mm. The mode stirrer

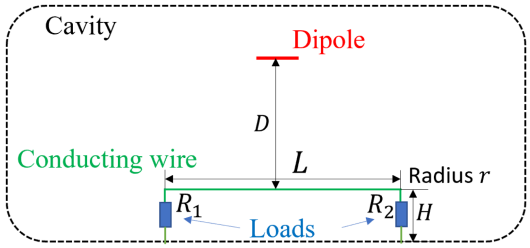

Fig. 9. Illustration of the radiated dipole and conducting wire.

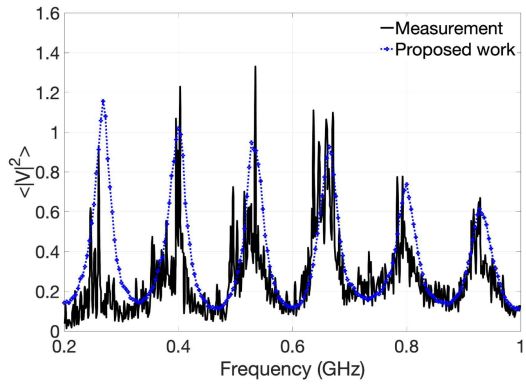

Fig. 10. Mean of the squared magnitude of coupled voltage.

is rotated in steps of 10 degrees for a frequency range from 200 to 1000 MHz in steps of 1 MHz.

To replicate such a testing environment using the proposed work, a simulation setup shown in Fig. 9 is designed. The length L, height H, and radius r are the same as the experimental setting. The wire is terminated with $R_1 = R_2 = 50\,\Omega$ at both ends. A small dipole antenna is utilized to generate the stochastic field inside the cavity. By placing the dipole far away from the conducting wire, $(kD \gg 1)$, we can utilize the S-DGF to calculate the power density of radiated diffusive field as: $\langle |\mathbf{E}|^2 \rangle = \frac{\omega^2 \mu^2 Q (I_0\, l)^2}{24\pi k V}$. Next, based on the chamber constant ([67, Fig. 3]) and quality factor (Fig. 4 in [68]), we can retrieve the dipole current $I_0\, l$ that is needed to generate the same statistical cavity environment.

Both the dipole and the conducting wire are treated using the EFIE [66] with the S-DGF as the kernel. A set of $5\,\mathrm{k}$ Gaussian Orthogonal Ensemble (GOE) random matrices with dimensions of 2000×2000 are used to generate an ensemble of S-DGF EFIE matrices. As a result, $5\,\mathrm{k}$ induced voltage samples at the wire terminal across R_2 are computed. The mean of the squared magnitude $\langle |V|^2 \rangle$ is compared with the measurements [67] in Fig. 10. Good agreement is observed.

C. Experimental Validation

Next, we experimentally validate the proposed work using a complex wave scattering environment. Fig. 11 illustrates the testing environment of an aluminum box (of length $1.27\ \mathrm{m}$, width $1.22\ \mathrm{m}$, and height $0.65\ \mathrm{m}$) with irregular internal scatterers and a conducting paddle stirrer. Two monopole antennas with electrical length $\lambda/3$ at frequency 6.45 GHz are mounted on

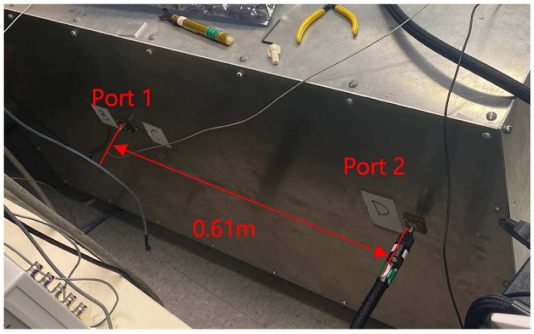

(a)

(b)

Fig. 11. Configuration of the cavity testing environment. (a) Exterior view. (b) Interior view.

the cavity wall as transmitter (Tx) and receiver (Rx). As shown in Fig. 11, they are separated over a distance of $L = 0.61$ m, which is about 13.12 λ.

In the measurement setup, both monopole antennas are connected to the N5242 A PNA-X Microwave Network Analyzer. The paddle-wheel mode stirrer that is controlled by a LabVIEW program rotates 200 positions over 360 degrees. A total number of 20-k S-parameter measurements are collected from 6.44 to 6.45 GHz with 0.1 MHz frequency stepping. In the simulation setup, the volume of the cavity is calculated as 1.0071 m^3 and the estimated cavity loss-parameter $\alpha = 10.16$. A total set of 20-k GOE random matrices with dimensions of 2000×2000 are used to generate S-DGF IE matrices. Therefore, 20-k S-parameter samples are computed with the proposed work. The PDFs of S-parameter amplitudes, $|\mathrm{S}_{11}|$ and $|\mathrm{S}_{12}|$, are compared to the measurement result in Fig. 12. A good agreement is observed.

To validate the proposed work in the case of coherent coupling, we adjust the distance between the two monopole antennas as 3.16 cm (i.e., 0.68 λ), as shown in Fig. 13. Since these two antennas are close to each other, we expect an increase of the coherent coupling component, which leads to a greater mean value of the S_{12} parameter. The comparison of measurement and simulation results are shown in Fig. 14. The results again agree very well.

D. Aperture Coupling From External Plane Wave

Finally, we consider a numerical study of aperture coupling from the external incident plane wave. A PEC enclosure of cuboid shape with three apertures on the cavity wall was chosen as the test case. The configuration of the cavity is shown in Fig. 15. The dimension of the cavity is $[-0.5\,\mathrm{m}, 0.5\,\mathrm{m}]$:$[-0.5\,\mathrm{m}, 0.5\,\mathrm{m}]$:$[-0.5\,\mathrm{m}, 0.5\,\mathrm{m}]$ in length, width, and height. Three apertures with circular shape, square shape, and rectangular shape are located in the *xy* plane, *yz* plane, and *xz* plane, respectively. The radius of the circular aperture is 0.1 m. The size of the square aperture is 0.2 by 0.2 m. And the size of the rectangular aperture is 0.1 by 0.3 m. An irregular Z-folded stirrer is introduced to emulate complex

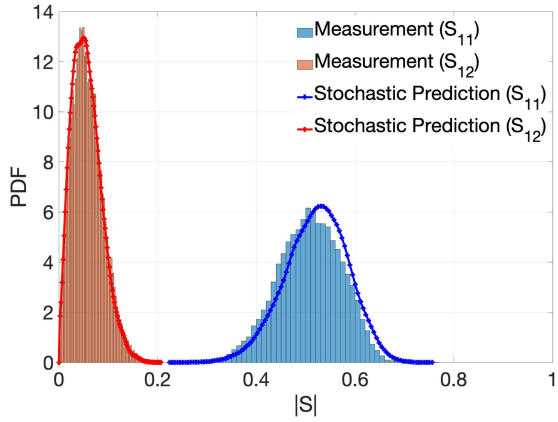

Fig. 12. PDFs of $|\mathrm{S}_{11}|$ and $|\mathrm{S}_{12}|$.

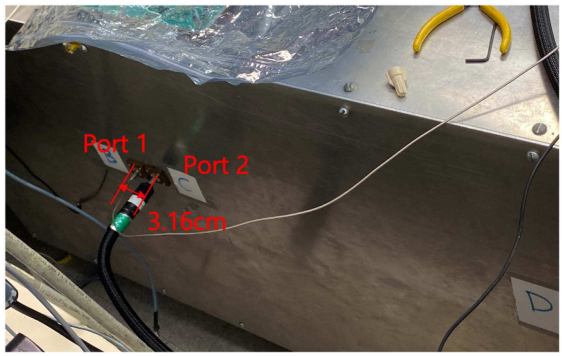

Fig. 13. Measurement configuration of nearby antennas.

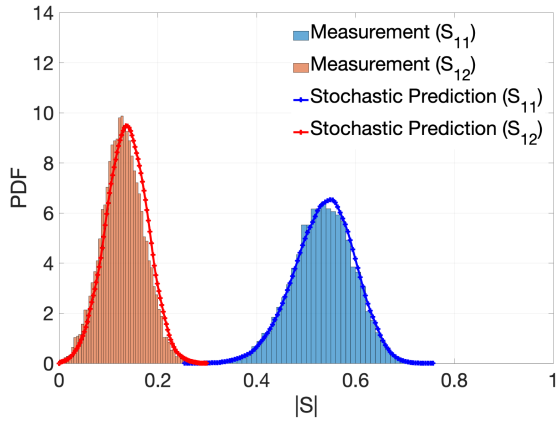

Fig. 14. PDFs of $|\mathrm{S}_{11}|$ and $|\mathrm{S}_{12}|$ for nearby antennas.

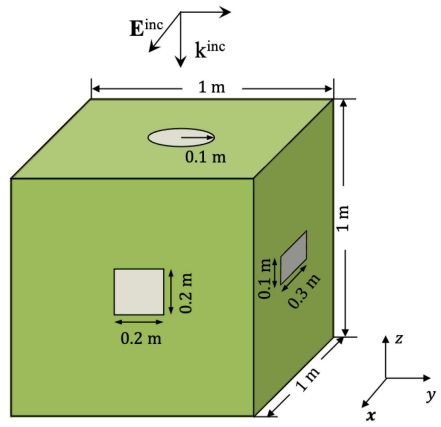

(a)

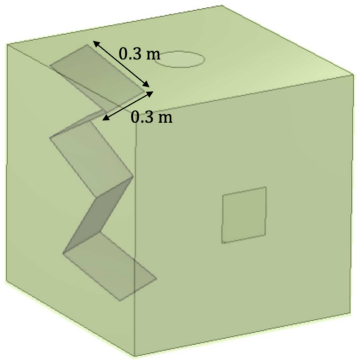

(b)

Fig. 15. Configuration of the cavity with apertures and stirrer.

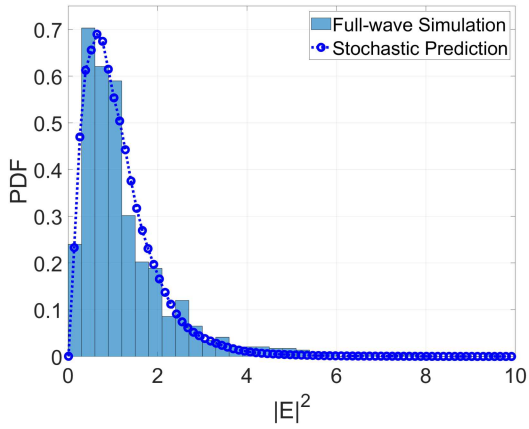

(a)

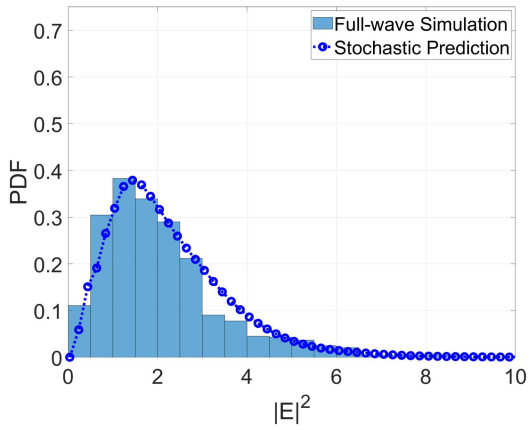

(b)

Fig. 16. PDF of the amplitude square of electric field at two probe locations.

internal structures inside realistic cavities [69], [70]. The stirrer has five 0.3 by 0.3-m metallic plates that are arranged in different folding angles, as shown in Fig. 15(b). The center of the stirrer is located at $\underline{x} = -0.25$ m and $y = -0.25$ m. The enclosure is illuminated by an external plane wave at 1 GHz. The incident wave vector is k=$(0, 0, -1)$, and the electric field is along the x direction.

Our goal is to predict the statistics of coupled internal electric field density at specific locations. Two probe locations are selected as: P1=$(0.15\,\mathrm{m}, 0\,\mathrm{m}, -0.15\,\mathrm{m})$, and P2=$(0.05\,\mathrm{m}, 0\,\mathrm{m}, 0.4\,\mathrm{m})$. It is noted that the P2 location is much closer to the illuminated aperture than the P1. Thereby, a stronger coherent coupling should be expected.

The statistical prediction consists of two steps. The first one is to estimate the cavity quality factor and the loss parameter α. As there are no internal losses inside the cavity, the quality factor is determined by the power loss due to the aperture leakage only. Consider a plane wave impinging on the wall aperture, the power leakage problem can be solved by the EFIE method formulated on the aperture surface. The leakage power is calculated by integrating the Poynting vector over the surface of the aperture. Next, the parameter of leakage cross-section σ_{lkg} is calculated by dividing the leakage power with incident power [11]. In the context of random superposition of plane waves in cavity environments, the mean leakage cross-section, $\langle\sigma_{\mathrm{lkg}}\rangle$, is obtained by averaging the leakage cross-section for many plane wave incidence angles and polarizations in the angular domain. Together with the volume of the chassis, i.e., $V = 1\,\mathrm{m}^3$, the quality factor is obtained as $Q = 984.5$ and the loss-parameter $\alpha = 0.473$.

We can then utilize the calculated loss-parameter $\alpha = 0.473$ to generate the S-DGF IE matrices in (65). A total set of 10-k GOE random matrices with dimensions of 2000×2000 are used to generate S-DGF IE matrices. Therefore, a total number of 10-k electric field samples at locations P1 and P2 are computed with the proposed work.

To validate the statistical prediction, we have conducted the full-wave simulation utilizing the CST software. In the CST simulation setup, the mode stirrer is rotated through 12 positions over 360 degrees. At each stirrer position, an ensemble of electric fields for the specific pickups is generated from 0.99 to 1.01 GHz with 0.25-MHz increment. Thus, a total number of 972 electric field samples are collected for each location point in the experiment. The statistical prediction and the full-wave simulation results are presented in Fig. 16. It is noted that the CST full-wave simulations were limited to 12 stirrer configurations, which result in coarser resolution in the histograms.

Both the stochastic and full-wave simulations were conducted on a workstation with Intel Xeon silver 4114 CPU and 208 GB of

memory. The construction of 10-k S-DGF IE matrices took 26.2 min, and the solution of the IE matrices was obtained in 7 min. Regarding the full-wave simulations of 12 cavity configurations, each simulation took 5 h and 15 min on average. Thereby, a total time of 3780 min is required to obtain the results of the configuration ensemble.

IV. Conclusion

In this article, we have proposed a sS-DGF method as an effective statistical solution to the vector wave equation in large, complex enclosures. The S-DGF is based on a statistical description of the eigenmodes of an enclosed EM environment. The eigenfunction statistics are derived from the vector random wave model, taking into account different orientations of polarization. A tensor representation of field-field correlation is utilized for the transversal and longitudinal field-field correlations. The eigenvalues statistics are generated by the Wigner's random matrix theory.

As a statistical wave model, the S-DGF self-consistently characterizes coherent and incoherent propagations from the vector EM source to the vector EM field using generic, macroscopic parameters of the cavity environment. By analogy with the standard Green's function in a deterministic environment, we expect the S-DGF to play an important role in the numerical modeling of the vector wave equation in confined EM environments.

Applicationwise, the work can be used for the study of antennas and electronics within large and complicated enclosures, such as EMC testing in reverberation chambers and wireless networks in industrial environments. In the context of IEMI coupling, the work serves as a physics-oriented computational model, which integrated the deterministic (POEs and POIs) and statistical (cavity interior) attributes in a rigorous and comprehensive way. Such a modeling capability is valuable for predicting intentional interference, assessing vulnerabilities, protecting sensitive electronics, and developing frequency-agile waveforms.

Our future work is devoted to expanding the S-DGF method from the spatial domain to the space-wavenumber domain and the space-time domain. The research goal is to accomplish a computational statistical model for the temporal, spectral, and spatial characteristics of wave physics in large, complex enclosures.

Appendix A

A. Derivation of the Dyadic Green's Function Using Eigenfunction Expansion

Consider the second-order vector wave equation

$$\nabla \times \nabla \times \mathbf{E}(\mathbf{r}) - \tilde{k}^2 \mathbf{E}(\mathbf{r}) = -j\omega\mu_0 \mathbf{J}(\mathbf{r}') \tag{68}$$

where $\tilde{k}^2$ is the square of complex wave number, defined by

$$\tilde{k}^2 = \omega^2\mu_0\epsilon - j\omega\mu_0\sigma = k^2 - jk^2/Q. \tag{69}$$

The vector DGF satisfies

$$\nabla \times \nabla \times \overline{\overline{\mathbf{G}}}(\mathbf{r}, \mathbf{r}') - \tilde{k}^2 \overline{\overline{\mathbf{G}}}(\mathbf{r}, \mathbf{r}') = -\overline{\overline{\mathbf{I}}}\delta(\mathbf{r} - \mathbf{r}'). \tag{70}$$

According to the nomenclature of dyadic analysis, $\overline{\overline{\mathbf{I}}}$ is the unit dyad (idemfactor), which can be decomposed into $\hat{\mathbf{x}}\hat{\mathbf{x}} + \hat{\mathbf{y}}\hat{\mathbf{y}} + \hat{\mathbf{z}}\hat{\mathbf{z}}$. Therefore, the DGF $\overline{\overline{\mathbf{G}}}$ can be also decomposed into three vector components $\mathbf{G}_m$ with $m = (x, y, z)$, satisfying

$$\nabla \times \nabla \times \mathbf{G}_m(\mathbf{r}, \mathbf{r}') - \tilde{k}^2 \mathbf{G}_m(\mathbf{r}, \mathbf{r}') = -\hat{\mathbf{m}}\delta(\mathbf{r} - \mathbf{r}'). \tag{71}$$

We remark that $\mathbf{G}_m(\mathbf{r}, \mathbf{r}')$ represents the vector electric field due to an infinitesimal electric dipole oriented in the direction of $\hat{\mathbf{m}}$ and located at $\mathbf{r}'$.

To solve (71), we expand $\mathbf{G}_m(\mathbf{r}, \mathbf{r}')$ in the basis of the eigenfunctions of the cavity with PEC boundary condition, i.e., $\mathbf{G}_m(\mathbf{r}, \mathbf{r}') = \sum_i C_i^m \Psi_i(\mathbf{r}, k_i)$, where

$$\nabla \times \nabla \times \Psi_i(\mathbf{r}, k_i) - k_i^2 \Psi_i(\mathbf{r}, k_i) = 0 \quad \text{in volume } V \tag{72}$$

$$\hat{\mathbf{n}} \times \Psi_i(\mathbf{r}, k_i) = 0 \quad \text{on boundary } S. \tag{73}$$

The eigenfunctions are orthogonal, $\langle \Psi_i(\mathbf{r}, k_i), \Psi_j(\mathbf{r}, k_j) \rangle = \delta_{ij}$, with respect to the inner product

$$\langle \mathbf{u}, \mathbf{v} \rangle = \int_V \mathbf{u} \cdot \mathbf{v} dV. \tag{74}$$

Next, testing (71) with $\Psi_i(\mathbf{r}, k_i)$ yields

$$C_i^m = \sum_i \frac{\hat{\mathbf{m}}\Psi_i(\mathbf{r}', k_i)}{\tilde{k}^2 - k_i^2}, \ \hat{\mathbf{m}} = (\hat{\mathbf{x}}, \hat{\mathbf{y}}, \hat{\mathbf{z}}). \tag{75}$$

Then we have

$$\mathbf{G}_m(\mathbf{r}, \mathbf{r}') = \sum_i \frac{\Psi_i(\mathbf{r}, k_i)\, \hat{\mathbf{m}}\Psi_i(\mathbf{r}', k_i)}{\tilde{k}^2 - k_i^2}. \tag{76}$$

By utilizing (76) and the definition of tensor product, we obtain the DGF in the form of $\overline{\overline{\mathbf{G}}}(\mathbf{r}, \mathbf{r}') = \sum_m \mathbf{G}_m(\mathbf{r}, \mathbf{r}')\hat{\mathbf{m}}$, which leads to the expression in (4).

B. Variance of the Cavity Eigenfunction

To derive the variance of eigenfunctions $\Psi_i(\mathbf{r})$, we recall that the polarization angle ψ_n in the vector components is uniformly distributed in $[0, 2\pi]$. We first calculate the variance of the spherical vector component by

$$\begin{aligned}\left\langle \Psi_i^\theta(\mathbf{r}), \Psi_i^\theta(\mathbf{r}) \right\rangle &= \frac{1}{2\pi} \int_0^{2\pi} \cos^2\psi_n d\psi_n \times \frac{2}{V} \frac{1}{4\pi} \\ &\quad \int_0^{\pi} \int_0^{2\pi} \cos^2(k_i \hat{\mathbf{e}}_n \cdot \mathbf{r} + \beta_n) \, d\phi \sin\theta d\theta \\ &= \frac{1}{2} \times \frac{1}{V} = \frac{1}{2V}.\end{aligned}$$

Similarly, we can obtain

$$\left\langle \Psi_i^\phi(\mathbf{r}), \Psi_i^\phi(\mathbf{r}) \right\rangle = \frac{1}{2V}$$

$$\left\langle \Psi_i^\theta(\mathbf{r}), \Psi_i^\phi(\mathbf{r}) \right\rangle = \left\langle \Psi_i^\phi(\mathbf{r}), \Psi_i^\theta(\mathbf{r}) \right\rangle = 0.$$

Thus, the resulting variance of eigenfunctions $\Psi_i(\mathbf{r})$ can be calculated by

$$\langle \Psi_i(\mathbf{r}), \Psi_i(\mathbf{r}) \rangle = \left\langle \Psi_i^\theta(\mathbf{r}), \Psi_i^\theta(\mathbf{r}) \right\rangle + \left\langle \Psi_i^\phi(\mathbf{r}), \Psi_i^\phi(\mathbf{r}) \right\rangle$$

$$+\left\langle \Psi_i^{\theta}(\mathbf{r}), \Psi_i^{\phi}(\mathbf{r}) \right\rangle + \left\langle \Psi_i^{\phi}(\mathbf{r}), \Psi_i^{\theta}(\mathbf{r}) \right\rangle = \frac{1}{V}.$$

Next, we show that the same result can be obtained using the Cartesian coordinate expression in (8). To simplify the expression, we assume the direction $\hat{\mathbf{e}}_n$ and $\mathbf{r}$ are located at x-y plane. We first calculate the variance of the vector component by

$$\begin{aligned}\left\langle \Psi_i^x(\mathbf{r}), \Psi_i^x(\mathbf{r}) \right\rangle &= \frac{1}{2}\int_0^{\pi}\frac{1}{2\pi}\int_0^{2\pi}\frac{1}{2\pi}\int_0^{2\pi}\left[\cos^2\psi_n \sin^2\phi_n \right.\\ &\left. + \sin^2\psi_n \cos^2\phi_n \cos^2\theta\right] d\psi_n d\phi_n \sin\theta d\theta\\ &\times \frac{2}{V}\frac{1}{2\pi}\int_0^{2\pi}\cos^2\left(k_i\hat{\mathbf{e}}_n\cdot\mathbf{r}+\beta_n\right)d\phi\\ &= \left(\frac{1}{2}\times\frac{1}{2}\times 1+\frac{1}{2}\times\frac{1}{2}\times\frac{1}{3}\right)\times\frac{1}{V}\\ &= \frac{1}{3V}.\end{aligned}$$

Similarly, we have for the result of the y component. The derivation of the z component is given by

$$\begin{aligned}\left\langle \Psi_i^z(\mathbf{r}), \Psi_i^z(\mathbf{r}) \right\rangle &= \frac{1}{2\pi}\int_0^{2\pi}\sin^2\psi_n d\psi_n \times \frac{1}{2}\int_0^{\pi}\sin^3\theta d\theta\\ &\times \frac{2}{V}\frac{1}{2\pi}\int_0^{2\pi}\cos^2\left(k_i\hat{\mathbf{e}}_n\cdot\mathbf{r}+\beta_n\right)d\phi\\ &= \frac{1}{2}\times\frac{2}{3}\times\frac{1}{V}\\ &= \frac{1}{3V}.\end{aligned}$$

C. Autocorrelation of Eigenfunctions

As illustrated in Fig. 1, the covariance function of longitudinal vector components can be calculated by

$$\begin{aligned}&\left\langle \Psi_i^z(\mathbf{r}), \Psi_i^z(\mathbf{r}') \right\rangle\\ &= \frac{2}{V}\left\langle \sin^2\psi_n \sin^2\theta_n \cos\left(k_i\hat{\mathbf{e}}_n\cdot\mathbf{r}+\beta_n\right)\cos\left(k_i\hat{\mathbf{e}}_n\cdot\mathbf{r}'+\beta_n\right)\right\rangle\\ &= \frac{1}{V}\left\langle \sin^2\psi_n \sin^2\theta_n\left[\cos(k_i\hat{\mathbf{e}}_n\cdot\hat{\mathbf{z}}R)+\cos(k_i\hat{\mathbf{e}}_n\cdot(\mathbf{r}+\mathbf{r}')+2\beta_n)\right]\right\rangle\\ &= \frac{1}{V}\frac{1}{2\pi}\int_0^{2\pi}\sin^2\psi_n d\psi_n \times \frac{1}{2}\int_0^{\pi}\sin^3\theta_n\cos\left(k_iR\cos\theta_n\right)d\theta_n\\ &= \frac{1}{4V}\int_{-1}^{1}\left(1-u^2\right)\cos\left(k_iRu\right)du\\ &= \frac{1}{V}\frac{\sin k_iR - k_iR\cos k_iR}{(k_iR)^3}\\ &= \frac{1}{3V}f_{//}\left(k_iR\right).\end{aligned}$$

Similarly, we could also derive the covariance function between transverse vector components

$$\begin{aligned}\left\langle \Psi_i^x(\mathbf{r}), \Psi_i^x(\mathbf{r}') \right\rangle &= \left\langle \Psi_i^y(\mathbf{r}), \Psi_i^y(\mathbf{r}') \right\rangle\\ &= \frac{2}{V}\left[\frac{\sin k_iR}{k_iR} - \frac{\sin k_iR - k_iR\cos k_iR}{(k_iR)^3}\right]\\ &= \frac{1}{3V}f_{\perp}\left(k_iR\right).\end{aligned}$$

D. Derivation of the Variance Var(g_{xz})

From (44), we introduce g_{xz} as

$$g_{xz} = \sum_m^M \frac{w_m^x (w_m^z)'}{\tilde{\lambda}_m - j\alpha} \tag{77}$$

where w_m^x and $(w_m^z)'$ are two independent, zero mean Gaussian random variables with the variance of $1/(3V)^2$. According to RMT, $\tilde{\lambda}_m$ follows uniform distribution in $[-M/2, M/2]$ ($M \gg 1$). Then, we have the PDF of $\tilde{\lambda}_m$ described by

$$f\left(\tilde{\lambda}_m\right) = \begin{cases}\frac{1}{M} & -\frac{M}{2} \le \tilde{\lambda}_m \le \frac{M}{2}\\ 0 & \text{otherwise.}\end{cases} \tag{78}$$

It is easy to prove that the mean $\langle g_{xz}\rangle = 0$, then the variance of g_{xz} can be derived as

$$\begin{aligned}\mathrm{Var}\left(g_{xz}\right) &= \left\langle |g_{xz}|^2 \right\rangle = \left\langle \sum_m^M \frac{\{w_m^x (w_m^z)'\}^2}{\tilde{\lambda}_m^2 + \alpha^2} \right\rangle\\ &= \frac{1}{9V^2}\sum_m^M \frac{1}{\tilde{\lambda}_m^2 + \alpha^2}.\end{aligned}$$

Based on the Monte Carlo integration, we have

$$\begin{aligned}\sum_m^M \frac{1}{\tilde{\lambda}_m^2 + \alpha^2} &\approx \int_{-M/2}^{M/2}\frac{d\tilde{\lambda}_m}{\tilde{\lambda}_m^2 + \alpha^2} \approx \int_{-\infty}^{\infty}\frac{d\tilde{\lambda}_m}{\tilde{\lambda}_m^2 + \alpha^2}\\ &= \frac{\arctan\left(\tilde{\lambda}_m/\alpha\right)}{\alpha}\Bigg|_{-\infty}^{\infty} = \frac{\pi}{\alpha}.\end{aligned}$$

Thus, we have $\mathrm{Var}(g_{xz}) = \pi/(9V^2\alpha)$. Fig. 17 shows the variance of g_{xz} with increasing α (assuming $1/(9V^2) = 1$), where a good agreement is observed as expected. Similarly, we can also obtain $\mathrm{Var}(g_{yz}) = \pi/(9V^2\alpha)$ and $\mathrm{Var}(g_{zz}) = 2\pi/(9V^2\alpha)$, where g_{yz} and g_{zz} are introduced in (45) and (46), respectively.

E. Derivation of Eigenfunctions Close to Boundary

Consider the RPW approximation of eigenfunction in (49), the variance of normal vector components is calculated by

$$\begin{aligned}&\left\langle \hat{\mathbf{z}}\cdot\boldsymbol{\Psi}_i^{\mathrm{e}}(\mathbf{r}), \hat{\mathbf{z}}\cdot\boldsymbol{\Psi}_i^{\mathrm{e}}(\mathbf{r}) \right\rangle\\ &= \left\langle \tilde{\Psi}_i^z(\mathbf{r}) + \tilde{\Psi}_i^z(\mathbf{r}_{\mathrm{i}}), \tilde{\Psi}_i^z(\mathbf{r}) + \tilde{\Psi}_i^z(\mathbf{r}_{\mathrm{i}}) \right\rangle\\ &= \left\langle \left[\tilde{\Psi}_i^z(\mathbf{r})\right]^2 + \left[\tilde{\Psi}_i^z(\mathbf{r}_{\mathrm{i}})\right]^2 + 2\tilde{\Psi}_i^z(\mathbf{r})\,\tilde{\Psi}_i^z(\mathbf{r}_{\mathrm{i}}) \right\rangle.\end{aligned} \tag{79}$$

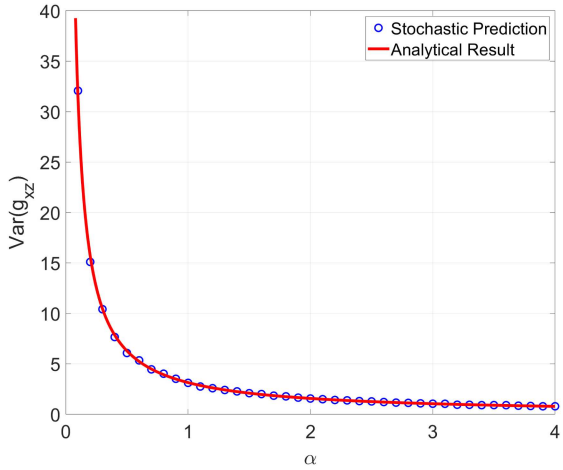

Fig. 17. Variance of g_{xz} with increasing α.

Since $\left\langle \tilde{\Psi}_i^z, \tilde{\Psi}_i^z \right\rangle = \langle \Psi_i^z, \Psi_i^z \rangle / 2$, we have the results of the first two items

$$\left\langle \left[\tilde{\Psi}_i^z(\mathbf{r})\right]^2 + \left[\tilde{\Psi}_i^z(\mathbf{r}_\mathrm{i})\right]^2 \right\rangle = \frac{1}{3V}. \tag{80}$$

One can derive the third cross term through a similar procedure in Appendix C

$$2\left\langle \tilde{\Psi}_i^z(\mathbf{r}), \tilde{\Psi}_i^z(\mathbf{r}_\mathrm{i}) \right\rangle = \frac{1}{3V} f_{//}(k_i h). \tag{81}$$

By substituting (80) and (81) into (79), the variance of normal vector component in (52) can be obtained. The derivation of the variance in tangential vector components follows a similar procedure and is skipped herein.

F. Finite Dimensional Discretization of Aperture SIE Matrices

To obtain the discrete system of (64), the aperture surface S_a is discretized by a collection of triangular meshes denoted by $\mathcal{K}^h$. Both trial and test functions utilize the surface div-conforming vector Rao–Wilton–Glisson (RWG) functions [71], λ^h, which are defined over $\mathcal{K}^h$.

By substituting (58) and (62) into (63), we have

$$2\pi_\tau\left(\iint_{S_a} \overline{\overline{\mathbf{G}}}_0(\mathbf{r},\mathbf{r}')\cdot\mathbf{M}(\mathbf{r}')\,dS'\right) + \pi_\tau\left(\iint_{S_a} \overline{\overline{\mathbf{G}}}_S^{\mathrm{h,m}}(\mathbf{r},\mathbf{r}')\cdot\mathbf{M}(\mathbf{r}')\,dS'\right) = 2\frac{j\eta}{k_0}\mathbf{H}_t^{\mathrm{inc}}(\mathbf{r}). \tag{82}$$

The right-hand-side (RHS) vector in (64) can be calculated by applying the RWG testing function

$$\overline{\mathbf{H}}^{\mathrm{inc}} = \iint_{\mathcal{K}^h} \lambda^h(\mathbf{r})\cdot 2\frac{j\eta}{k_0}\mathbf{H}_t^{\mathrm{inc}}(\mathbf{r})\,dS. \tag{83}$$

The aperture admittance matrix for the exterior subregion using the free-space DGF reads

$$\mathbf{Y}_0^{\mathrm{h,m}} = 2\iint_{\mathcal{K}^h}\iint_{\mathcal{K}^h} \lambda^h(\mathbf{r})\cdot\left[\pi_\tau\left(\overline{\overline{\mathbf{G}}}_0(\mathbf{r},\mathbf{r}')\right)\cdot\lambda^h(\mathbf{r}')\right]dS'dS. \tag{84}$$

Next, we will derive the aperture admittance matrix of the interior subregion. At the aperture surface, the magnetic field eigenfunction, $\mathbf{\Psi}_i^{\mathrm{h}}(\mathbf{r})$, in (60) reduces to

$$\mathbf{\Psi}_i^{\mathrm{h}}(\mathbf{r}) \simeq 2\tilde{\Psi}_i^x(\mathbf{r})\,\hat{\mathbf{x}} + 2\tilde{\Psi}_i^y(\mathbf{r})\,\hat{\mathbf{y}} \quad \text{on } S_a. \tag{85}$$

Similarly, from the expression of source eigenfunction, $\mathbf{\Psi}_i^{\mathrm{m}}(\mathbf{r}')$, in (61), we have

$$\mathbf{\Psi}_i^{\mathrm{m}}(\mathbf{r}') \simeq 2\tilde{\Psi}_i^x(\mathbf{r}')\,\hat{\mathbf{x}} + 2\tilde{\Psi}_i^y(\mathbf{r}')\,\hat{\mathbf{y}} \quad \text{on } S_a. \tag{86}$$

The outer product of $\mathbf{\Psi}_i^{\mathrm{h}}(\mathbf{r})$ and $\mathbf{\Psi}_i^{\mathrm{m}}(\mathbf{r}')$ on S_a gives rise to

$$\begin{aligned}
&\mathbf{\Psi}_i^{\mathrm{h}}(\mathbf{r}) \otimes \mathbf{\Psi}_i^{\mathrm{m}}(\mathbf{r}') \\
&= 2\Psi_i^x(\mathbf{r})\,\Psi_i^x(\mathbf{r}')\,\hat{\mathbf{x}}\hat{\mathbf{x}} + 2\Psi_i^x(\mathbf{r})\,\Psi_i^y(\mathbf{r}')\,\hat{\mathbf{x}}\hat{\mathbf{y}} \\
&\quad + 2\Psi_i^y(\mathbf{r})\,\Psi_i^x(\mathbf{r}')\,\hat{\mathbf{y}}\hat{\mathbf{x}} + 2\Psi_i^y(\mathbf{r})\,\Psi_i^y(\mathbf{r}')\,\hat{\mathbf{y}}\hat{\mathbf{y}} \\
&= 2\,\pi_\tau(\mathbf{\Psi}_i(\mathbf{r})) \otimes \pi_\tau(\mathbf{\Psi}_i(\mathbf{r}'))
\end{aligned} \tag{87}$$

where the $\mathbf{\Psi}_i$ is the RPW with uniformly distributed orientation and polarization defined in (8).

As a result of the derivation that was introduced in Section II-B, the tangential component of the electric S-DGF of the second kind becomes

$$\pi_\tau\left(\overline{\overline{\mathbf{G}}}_S^{\mathrm{h,m}}(\mathbf{r},\mathbf{r}')\right) = \pi_\tau\left(2\mathrm{Re}\left[\overline{\overline{\mathbf{G}}}_0(\mathbf{r},\mathbf{r}')\right]\right) + \sum_m \frac{\pi_\tau\left(2\overline{\overline{\mathbf{D}}}(\mathbf{r},\mathbf{r}';k_m)\right)}{\tilde{\lambda}_m - j\alpha}\frac{kV}{2\pi^2}. \tag{88}$$

Accordingly, the aperture admittance matrix of the interior subregion consists of two parts. We have for the first part

$$\begin{aligned}
&\iint_{\mathcal{K}^h}\iint_{\mathcal{K}^h} \lambda^h(\mathbf{r})\cdot\left[\pi_\tau\left(2\mathrm{Re}\left[\overline{\overline{\mathbf{G}}}_0(\mathbf{r},\mathbf{r}')\right]\right)\cdot\lambda^h(\mathbf{r}')\right]dS'dS \\
&= \mathrm{Re}\left[\mathbf{Y}_0^{\mathrm{h,m}}\right].
\end{aligned} \tag{89}$$

Regarding the second part, we first check the outer product in the numerator with trial and testing functions

$$\begin{aligned}
&\iint_{\mathcal{K}^h}\iint_{\mathcal{K}^h} \lambda^h(\mathbf{r})\cdot\left[\pi_\tau\left(2\overline{\overline{\mathbf{D}}}(\mathbf{r},\mathbf{r}';k_m)\right)\cdot\lambda^h(\mathbf{r}')\right]dS'dS \\
&= \iint_{\mathcal{K}^h}\iint_{\mathcal{K}^h} \lambda^h(\mathbf{r})\cdot[2\pi_\tau(\mathbf{\Psi}_m(\mathbf{r}))\otimes\pi_\tau(\mathbf{\Psi}_m(\mathbf{r}'))]\cdot\lambda^h(\mathbf{r}')dS'dS \\
&= \iint_{\mathcal{K}^h}\iint_{\mathcal{K}^h} 2\left[\lambda^h(\mathbf{r})\cdot\pi_\tau(\mathbf{\Psi}_m(\mathbf{r}))\right]\left[\pi_\tau(\mathbf{\Psi}_m(\mathbf{r}'))\cdot\lambda^h(\mathbf{r}')\right]dS'dS \\
&= 2\iint_{\mathcal{K}^h} \lambda^h(\mathbf{r})\cdot\pi_\tau(\mathbf{\Psi}_m(\mathbf{r}))dS \iint_{\mathcal{K}^h} \pi_\tau(\mathbf{\Psi}_m(\mathbf{r}'))\cdot\lambda^h(\mathbf{r}')dS'.
\end{aligned} \tag{90}$$

From the property of RPW approximation, it is easy to show that both $[\lambda^h(\mathbf{r})\cdot\pi_\tau(\mathbf{\Psi}_m(\mathbf{r}))]$ and $[\pi_\tau(\mathbf{\Psi}_m(\mathbf{r}'))\cdot\lambda^h(\mathbf{r}')]$ satisfy the Gaussian distribution. The matrix entries in (90) are the result of a product of the Gaussian random variables, whose covariance function [after multiplying the remaining coefficient $\frac{kV}{2\pi^2}$ in (88)]

is expressed by

$$
\begin{aligned}
&< \iint_{\mathcal{K}^h} \iint_{\mathcal{K}^h} \lambda^h(\mathbf{r}) \cdot \left[\pi_\tau \left(2\overline{\overline{\mathbf{D}}}(\mathbf{r}, \mathbf{r}'; k_m) \right) \frac{kV}{2\pi^2} \cdot \lambda^h(\mathbf{r}') \right] dS' dS > \\
&= \iint_{\mathcal{K}^h} \iint_{\mathcal{K}^h} \lambda^h(\mathbf{r}) \cdot < \pi_\tau \left(2\overline{\overline{\mathbf{D}}}(\mathbf{r}, \mathbf{r}'; k_m) \right) > \frac{kV}{2\pi^2} \cdot \lambda^h(\mathbf{r}') dS' dS \\
&\approx \iint_{\mathcal{K}^h} \iint_{\mathcal{K}^h} \lambda^h(\mathbf{r}) \cdot \left[\pi_\tau \left(-\frac{2}{\pi} \mathrm{Im} \left[\overline{\overline{\mathbf{G}}}_0 (\mathbf{r}, \mathbf{r}') \right] \right) \cdot \lambda^h(\mathbf{r}') \right] dS' dS \\
&= -\frac{1}{\pi} \mathrm{Im} \left[\mathbf{Y}_0^{\mathrm{h,m}} \right].
\end{aligned}
$$

In the above derivation, we have used the result of (32) and the fact of $k_m \approx k$. Then, the correlated Gaussian random variables associated with individual RWG functions can be constructed using the discrete Karhunen–Loeve expansion

$$
[\tilde{\boldsymbol{w}}_m] = \sqrt{-\frac{1}{\pi} \mathrm{Im} \left[\mathbf{Y}_0^{\mathrm{h,m}} \right]} \, [\boldsymbol{w}_m] \,. \tag{91}
$$

Finally, the aperture admittance matrix of the interior subregion is written as

$$
\mathbf{Y}_S^{\mathrm{h,m}} = \mathrm{Re} \left[\mathbf{Y}_0^{\mathrm{h,m}} \right] + \sum_m \frac{\tilde{\boldsymbol{w}}_m \tilde{\boldsymbol{w}}_m^T}{\tilde{\lambda}_m - j\alpha}. \tag{92}
$$

A statistical ensemble of admittance matrix $\mathbf{Y}_S^{\mathrm{h,m}}$ can be acquired by repeatedly applying (92) to different GOE random matrices.

ACKNOWLEDGMENT

The authors would like to sincerely appreciate all valuable comments and suggestions from anonymous reviewers, which helped to improve the quality of the paper.

REFERENCES

[1] D. A. Hill, "Plane wave integral representation for fields in reverberation chambers," *IEEE Trans. Electromagn. Compat.*, vol. 40, no. 3, pp. 209–217, Aug. 1998.

[2] R. Holland and R. John, *Statistical Electromagnetics*. Philadelphia, PA, USA: Taylor and Francis, 1999.

[3] J. Lefébvre, J. Hagen, D. Lecointe, and W. Tabbara, "Coupling of electromagnetic energy to a scatterer inside a cavity: A combined statistical and integral representation approach," *Radio Sci.*, vol. 35, no. 2, pp. 427–434, 2000.

[4] L. K. Warne, K. S. H. Lee, H. G. Hudson, W. A. Johnson, R. E. Jorgenson, and S. L. Stronach, "Statistical properties of linear antenna impedance in an electrically large cavity," *IEEE Trans. Antennas Propag.*, vol. 51, no. 5, pp. 978–992, May 2003.

[5] L. R. Arnaut, "Statistical distributions of dissipated power in electronic circuits immersed in a random electromagnetic field," *Radio Sci.*, vol. 40, pp. 1–10, Dec. 2005.

[6] S. Hemmady, X. Zheng, T. M. Antonsen, E. Ott, and S. M. Anlage, "Universal impedance fluctuations in wave chaotic systems," *Phys. Rev. Lett.*, vol. 94, no. 1, 2004, Art. no. 014102.

[7] S. Hemmady, X. Zheng, T. M. Antonsen, E. Ott, and S. M. Anlage, "Universal statistics of the scattering coefficient of chaotic microwave cavities," *Phys. Rev. E*, vol. 71, no. 5, 2005, Art. no. 056215.

[8] X. Zheng, T. Antonsen, E. Ott, and S. Anlage, "Statistics of impedance and scattering matrices in chaotic microwave cavities: Single channel cases," *Electromagnetics*, vol. 26, pp. 3–35, 2006.

[9] A. Gifuni, "On the expression of the average power received by an antenna in a reverberation chamber," *IEEE Trans. Electromagn. Compat.*, vol. 50, no. 4, pp. 1021–1022, Nov. 2008.

[10] H. W. L. Naus, "Statistical electromagnetics: Complex cavities," *IEEE Trans. Electromagn. Compat.*, vol. 50, no. 2, pp. 316–324, May 2008.

[11] D. A. Hill, *Electromagnetic Fields in Cavities: Deterministic and Statistical Theories*. Hoboken, NJ, USA: Wiley, 2009.

[12] A. Cozza, "Probability distributions of local modal-density fluctuations in an electromagnetic cavity," *IEEE Trans. Electromagn. Compat.*, vol. 54, no. 5, pp. 954–967, Oct. 2012.

[13] L. K. Warne and R. E. Jorgenson, "High-frequency electromagnetic scarring in three-dimensional axisymmetric convex cavities," *Electromagnetics*, vol. 36, no. 3, pp. 186–213, 2016.

[14] D. Hill, "Electronic mode stirring for reverberation chambers," *IEEE Trans. Electromagn. Compat.*, vol. 36, no. 4, pp. 294–299, Nov. 1994.

[15] L. Cappetta, M. Feo, V. Fiumara, V. Pierro, and M. Pinto, "Electromagnetic chaos in mode-stirred reverberation enclosures," *IEEE Trans. Electromagn. Compat.*, vol. 40, no. 3, pp. 185–192, Aug. 1998.

[16] V. Rajamani, C. F. Bunting, and J. C. West, "Stirred-mode operation of reverberation chambers for EMC testing," *IEEE Trans. Instrum. Meas.*, vol. 61, no. 10, pp. 2759–2764, Oct. 2012.

[17] L. Arnaut, "Mode-stirred reverberation chambers: A paradigm for spatio-temporal complexity in dynamic electromagnetic environments," *Wave Motion*, vol. 51, no. 4, pp. 673–684, 2014.

[18] J. C. West, R. Bakore, and C. F. Bunting, "Statistics of the current induced within a partially shielded enclosure in a reverberation chamber," *IEEE Trans. Electromagn. Compat.*, vol. 59, no. 6, pp. 2014–2022, Dec. 2017.

[19] P. Kildal and K. Rosengren, "Correlation and capacity of MIMO systems and mutual coupling, radiation efficiency, and diversity gain of their antennas: Simulations and measurements in a reverberation chamber," *IEEE Commun. Mag.*, vol. 42, no. 12, pp. 104–112, Dec. 2004.

[20] J. D. Sanchez-Heredia, J. F. Valenzuela-Valdes, A. M. Martinez-Gonzalez, and D. A. Sanchez-Hernandez, "Emulation of MIMO rician-fading environments with mode-stirred reverberation chambers," *IEEE Trans. Antennas Propag.*, vol. 59, no. 2, pp. 654–660, Feb. 2011.

[21] A. Marin-Soler et al., "Sample selection algorithms for enhanced MIMO antenna measurements using mode-stirred reverberation chambers," *IEEE Trans. Antennas Propag.*, vol. 60, no. 8, pp. 3892–3900, Aug. 2012.

[22] K. A. Remley et al., "Configuring and verifying reverberation chambers for testing cellular wireless devices," *IEEE Trans. Electromagn. Compat.*, vol. 58, no. 3, pp. 661–672, Jun. 2016.

[23] C. Bunting and S.-P. Yu, "Field penetration in a rectangular box using numerical techniques: An effort to obtain statistical shielding effectiveness," *IEEE Trans. Electromagn. Compat.*, vol. 46, no. 2, pp. 160–168, May 2004.

[24] R. Holland and R. St John, "Statistical response of EM-driven cables inside an overmoded enclosure," *IEEE Trans. Electromagn. Compat.*, vol. 40, no. 4, pp. 311–324, Nov. 1998.

[25] D. Fedeli, G. Gradoni, V. M. Primiani, and F. Moglie, "Accurate analysis of reverberation field penetration into an equipment-level enclosure," *IEEE Trans. Electromagn. Compat.*, vol. 51, no. 2, pp. 170–180, May 2009.

[26] S. Hemmady, T. Antonsen, E. Ott, and S. Anlage, "Statistical prediction and measurement of induced voltages on components within complicated enclosures: A wave-chaotic approach," *IEEE Trans. Electromagn. Compat.*, vol. 54, no. 4, pp. 758–771, Aug. 2012.

[27] G. Gradoni, T. M. Antonsen, and E. Ott, "Random coupling model for the radiation of irregular apertures," *Radio Sci.*, vol. 50, no. 7, pp. 678–687, 2015.

[28] M. Mehri and N. Masoumi, "Statistical prediction and quantification of radiated susceptibility for electronic systems PCB in electromagnetic polluted environments," *IEEE Trans. Electromagn. Compat.*, vol. 59, no. 2, pp. 498–508, Apr. 2017.

[29] G. Gradoni et al., "Wigner-function-based propagation of stochastic field emissions from planar electromagnetic sources," *IEEE Trans. Electromagn. Compat.*, vol. 60, no. 3, pp. 580–588, Jun. 2018.

[30] M. C. Gutzwiller, *Chaos in Classical and Quantum Mechanics (Interdisciplinary Applied Mathematics)*. New York, NY, USA: Springer, 1990.

[31] V. Galdi, I. Pinto, and L. Felsen, "Wave propagation in ray-chaotic enclosures: Paradigms, oddities and examples," *IEEE Antennas Propag. Mag.*, vol. 47, no. 1, pp. 62–81, Feb. 2005.

[32] G. Tanner and N. Sondergaard, "Wave chaos in acoustics and elasticity," *J. Phys. A: Math. Theor.*, vol. 40, no. 50, 2007, Art. no. R443.

[33] S. Moran, "The basics of electric weapons and pulsed-power technologies," *Leading Edge: Directed Energy Technol., Model. Assessment*, vol. 7, no. 4, pp. 50–57, 2012.

[34] S. Lin, Z. Peng, and T. M. Antonsen, "A stochastic Green's function for solution of wave propagation in wave-chaotic environments," *IEEE Trans. Antennas Propag.*, vol. 68, no. 5, pp. 3919–3933, May 2020.
[35] M. V. Berry, "Regular and irregular semiclassical wavefunctions," *J. Phys. A: Math. Gen.*, vol. 10, no. 12, 1977, Art. no. 2083.
[36] P. Cvitanovic, R. Artuso, R. Mainieri, G. Tanner, and G. Vattay, *Chaos: Classical and Quantum. ChaosBook.org, 2017. Version 15.9*.
[37] E. Wigner, "Random matrices in physics," *SIAM Rev.*, vol. 9, no. 1, pp. 1–23, 1967.
[38] V. E. Kravtsov, "Random matrix theory: Wigner-Dyson statistics and beyond. (Lecture notes of a course given at SISSA (Trieste, Italy))," 2009, *arXiv:0911.0639*.
[39] G. Gradoni, J.-H. Yeh, B. Xiao, T. M. Antonsen, S. M. Anlage, and E. Ott, "Predicting the statistics of wave transport through chaotic cavities by the random coupling model: A review and recent progress," *Wave Motion*, vol. 51, no. 4, pp. 606–621, 2014.
[40] J. Gil, Z. B. Drikas, T. D. Andreadis, and S. M. Anlage, "Prediction of induced voltages on ports in complex, three-dimensional enclosures with apertures, using the random coupling model," *IEEE Trans. Electromagn. Compat.*, vol. 58, no. 5, pp. 1535–1540, Oct. 2016.
[41] E. Ott, *Chaos in Dynamical Systems*, 2nd ed. Cambridge, U.K.: Cambridge Univ. Press, 2002.
[42] J. G. V. Bladel, *Electromagnetic Fields*. Piscataway, NJ, USA: IEEE Press, 2007, ch. 10, pp. 509–561.
[43] J. Stein, H.-J. Stöckmann, and U. Stoffregen, "Microwave studies of billiard Green functions and propagators," *Phys. Rev. Lett.*, vol. 75, pp. 53–56, Jul. 1995.
[44] T. H. Lehman, "A statistical theory of electromagnetic fields in complex cavities," *EMP Interaction Note 494*, 1993.
[45] E. Ott and W. M. Manheimer, "Cavity Q for ergodic eigenmodes," *Phys. Rev. A*, vol. 25, pp. 1808–1810, Mar. 1982.
[46] U. Kuhl, R. Höhmann, J. Main, and H.-J. Stöckmann, "Resonance widths in open microwave cavities studied by harmonic inversion," *Phys. Rev. Lett.*, vol. 100, no. 25, 2008, Art. no. 254101.
[47] L. R. Arnaut and G. Gradoni, "Probability distribution of the quality factor of a mode-stirred reverberation chamber," *IEEE Trans. Electromagn. Compat.*, vol. 55, no. 1, pp. 35–44, Feb. 2013.
[48] R. N. Clarke and C. B. Rosenberg, "Fabry-Perot and open resonators at microwave and millimetre wave frequencies, 2-300 GHz," *J. Phys. E: Sci. Instruments*, vol. 15, Jan. 1982, Art. no. 9.
[49] D. Hill, "Spatial correlation function for fields in a reverberation chamber," *IEEE Trans. Electromagn. Compat.*, vol. 37, no. 1, Feb. 1995, Art. no. 138.
[50] B. Eckhardt, U. Dörr, U. Kuhl, and H.-J. Stöckmann, "Correlations of electromagnetic fields in chaotic cavities," *Europhysics Lett.*, vol. 46, pp. 134–140, Apr. 1999.
[51] Y. Chien and K.-S. Fu, "On the generalized Karhunen-Loeve expansion (corresp.)," *IEEE Trans. Inf. Theory*, vol. 13, no. 3, pp. 518–520, Jul. 1967.
[52] A. Papoulis and S. U. Pillai, *Probability, Random Variables, and Stochastic Processes*, 4th ed. New York, NY, USA: McGraw-Hill Higher Education, 2002.
[53] C. T. Tai, *Dyadic Green Functions in Electromagnetic Theory*, 2nd ed. Piscataway, NJ, USA: IEEE Press, 1994.
[54] R. F. Harrington and J. R. Mautz, "Electromagnetic coupling through apertures by the generalized admittance approach," *Comput. Phys. Commun.*, vol. 68, no. 1, pp. 19–42, 1991.
[55] D. A. Hill, M. T. Ma, A. R. Ondrejka, B. F. Riddle, M. L. Crawford, and R. T. Johnk, "Aperture excitation of electrically large, lossy cavities," *IEEE Trans. Electromagn. Compat.*, vol. 36, no. 3, pp. 169–178, Aug. 1994.
[56] R. Araneo and G. Lovat, "Fast MoM analysis of the shielding effectiveness of rectangular enclosures with apertures, metal plates, and conducting objects," *IEEE Trans. Electromagn. Compat.*, vol. 51, no. 2, pp. 274–283, May 2009.
[57] A. Schroder et al., "Analysis of high intensity radiated field coupling into aircraft using the method of moments," *IEEE Trans. Electromagn. Compat.*, vol. 56, no. 1, pp. 113–122, Feb. 2014.
[58] G. Gradoni, T. M. Antonsen, S. M. Anlage, and E. Ott, "A statistical model for the excitation of cavities through apertures," *IEEE Trans. Electromagn. Compat.*, vol. 57, no. 5, pp. 1049–1061, Oct. 2015.
[59] Z. Peng, Y. Shao, H. Gao, S. Wang, and S. Lin, "High-fidelity, high-performance computational algorithms for intrasystem electromagnetic interference analysis of IC and electronics," *IEEE Trans. Compon. Packag. Manuf. Technol.*, vol. 7, no. 5, pp. 653–668, May 2017.
[60] I. Junqua, J.-P. Parmantier, and P. Degauque, "Field-to-wire coupling in an electrically large cavity: A semianalytic solution," *IEEE Trans. Electromagn. Compat.*, vol. 52, no. 4, pp. 1034–1040, Nov. 2010.
[61] R. S. Langley, "A reciprocity approach for computing the response of wiring systems to diffuse electromagnetic fields," *IEEE Trans. Electromagn. Compat.*, vol. 52, no. 4, pp. 1041–1055, Nov. 2010.
[62] M. Magdowski, S. V. Tkachenko, and R. Vick, "Coupling of stochastic electromagnetic fields to a transmission line in a reverberation chamber," *IEEE Trans. Electromagn. Compat.*, vol. 53, no. 2, pp. 308–317, May 2011.
[63] M. Magdowski and R. Vick, "Closed-form formulas for the stochastic electromagnetic field coupling to a transmission line with arbitrary loads," *IEEE Trans. Electromagn. Compat.*, vol. 54, no. 5, pp. 1147–1152, Oct. 2012.
[64] F. Vanhee, D. Pissoort, J. Catrysse, G. A. E. Vandenbosch, and G. G. E. Gielen, "Efficient reciprocity-based algorithm to predict worst case induced disturbances on multiconductor transmission lines due to incoming plane waves," *IEEE Trans. Electromagn. Compat.*, vol. 55, no. 1, pp. 208–216, Feb. 2013.
[65] H. Xie, J. F. Dawson, J. Yan, A. C. Marvin, and M. P. Robinson, "Numerical and analytical analysis of stochastic electromagnetic fields coupling to a printed circuit board trace," *IEEE Trans. Electromagn. Compat.*, vol. 62, no. 4, pp. 1128–1135, Aug. 2020.
[66] J. M. Jin, *Theory and Computation of Electromagnetic Fields*, 2nd ed. Hoboken, NJ, USA: Wiley, 2015.
[67] M. Magdowski, S. Siddiqui, and R. Vick, "Measurement of the stochastic electromagnetic field coupling into transmission lines in a reverberation chamber," in *Proc. ESA Workshop Aerosp. EMC*, 2012, pp. 1–6.
[68] M. Magdowski, B. R. Banjade, and R. Vick, "Measurement of the coupling to shielded cables above a ground plane in a reverberation chamber," in *Proc. Int. Symp. Electromagn. Compat.*, 2016, pp. 234–239.
[69] J. Clegg, A. Marvin, J. Dawson, and S. Porter, "Optimization of stirrer designs in a reverberation chamber," *IEEE Trans. Electromagn. Compat.*, vol. 47, no. 4, pp. 824–832, Nov. 2005.
[70] A. Ubin, R. Vogt-Ardatjew, F. Leferink, M. Z. Mohd Jenu, and S. Van De Beek, "Statistical analysis of three different stirrer designs in a reverberation chamber," in *Proc. Asia-Pacific Symp. Electromagn. Compat.*, 2015, pp. 604–607.
[71] S. M. Rao, D. R. Wilton, and A. W. Glisson, "Electromagnetic scattering by surfaces of arbitrary shape," *IEEE Trans. Antennas Propag.*, vol. AP-30, no. 3, pp. 409–418, May 1982.

Shen Lin (Student Member, IEEE) received the B.E. degree in optical and electronic information engineering and the M.S. degree in instrument and meter engineering from the Harbin Institute of Technology, Harbin, China, in 2012 and 2014, respectively, the M.S. degree in optical science and engineering from the University of New Mexico, Albuquerque, NM, USA, in 2019, and the Ph.D. degree in electrical and computer engineering from the University of Illinois at Urbana-Champaign (ECE ILLINOIS), Champaign, IL, USA, in 2022.

He is currently a Postdoctoral Fellow with ECE ILLINOIS. His research interests inlclude computational and statistical electromagnetics, stochastic electromagnetics, quantitative statistical analysis of IC and electronics in complex environments/systems, and nonparametric stochastic algorithms. His research work has an impact on electromagnetic interference and compatibility, signal and power integrity, and wireless communication. The goal is to create a strong bond between classical and quantum electrodynamic physics.

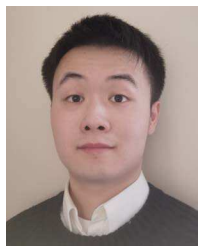

Sangrui Luo (Student Member, IEEE) received the B.S. degree in applied physics from the University of Science and Technology of China, Hefei, China in 2020. He is currently working toward the Ph.D. degree in electrical engineering with the Department of Electrical and Computer Engineering, University of Illinois at Urbana-Champaign, Champaign, IL, USA.

His research interests include computational electromagnetics and stochastic methods for wave-chaotic problems.

Shukai Ma (Student Member, IEEE) received the B.Sc. degree in applied physics from the University of Science and Technology of China, Hefei, China, in 2016, and the Ph.D. degree in physics from the University of Maryland, College Park, MD, USA, in 2022.

He is currently a R&D Hardware Engineer with the Wireless Semiconductor Division (WSD), Broadcom Inc., San Jose, CA, USA. His research interests include general complex phenomena in electromagnetic wave systems, and how machine learning techniques help us understand them, and RF device design and characterization.

Dr. Ma was the recipient of the Ann G. Wylie Dissertation Fellow at University of Maryland.

Junda Feng (Student Member, IEEE) received the B.S. degree in electronic information engineering from the Beijing Institute of Technology, Beijing, China, in 2020, and the M.S. degree in electrical and computer engineering from the University of Illinois at Urbana-Champaign, Champaign, IL, USA, in 2022.

His research interests include numerical and stochastic methods in computational electromagnetics and high-performance computing for partial differential equations.

Yang Shao (Member, IEEE) received the B.S. degree in electrical engineering and information science from the University of Science and Technology of China, Hefei, China, in 2003, and the Ph.D. degree in electrical engineering from the Chinese Academy of Sciences, Beijing, China, in 2008.

She was a Postdoctoral Researcher with the ElectroScience Laboratory, Ohio State University, Columbus, OH, USA, from 2009 to 2014, and a Research Assistant Professor with the Department of Electrical and Computer Engineering, University of New Mexico, Albuquerque, NM, USA, from 2014 to 2019. She is currently a Teaching Assistant Professor with the Department of Electrical and Computer Engineering, University of Illinois at Urbana-Champaign, Champaign, IL, USA. Her research interests include electromagnetic compatibility and scientific computing with a particular emphasis on the advancement of computational electromagnetics and computational thermal analysis. She has primarily been interested in the development of advanced mathematical formulations that may be used in conjunction with powerful numerical solvers to study real-world multiscale structures of integrated circuits, electronics, and antennas. She is also interested in multiphysics engineering application modeling and simulation-aided design, VLSI computer architectures, and multithreading microarchitectures.

Zachary B. Drikas (Member, IEEE) received the B.S. and M.S. degrees in electrical engineering (EE) from George Washington University, Washington, DC, USA, and the Ph.D. degree in EE from Virginia Tech, Blacksburg, VA, USA.

He has 13 years' experience with the U.S. Naval Research Laboratory's Tactical Electronic Warfare Division's high-power microwave (HPM) Section. He has (co)authored/invented 11 peer-reviewed journal articles, 43 invited reviews, 2 patent disclosures, 1 pending patent, 18 major DoD technical reports, 99 citations with an H-index of 6, 1 invited talk, 21 contributed talks. His research interests includes electromagnetic time-reversal techniques, advanced signal processing techniques, HPM effects on electronics/receiver systems, counter-directed energy applications, ultra-wideband (UWB) radar, and other UWB techniques.

Bisrat D. Addissie received the bachelor's, M.Sc., and Ph.D. degrees in electrical engineering from the University of Maryland, College Park, MD, USA, in 2010, 2015, and 2017, respectively. His dissertation was titled, "Methods for Characterizing Electromagnetic Coupling Statistics in Complex Enclosures."

From 2010 to 2016, he was a Researcher with the U.S. Food and Drug Administration's electromagnetic compatibility (EMC) laboratory, where he studied the susceptibility of personal electronic medical devices to nonionizing electromagnetic emissions from airport security systems. In 2017, he joined the Naval Research Laboratory, Washington, DC, USA, as an RF Engineer. He has authored and coauthored numerous reports and papers in peer-reviewed journals and conference proceedings. His research interests include statistical electromagnetics and electromagnetic time-reversal techniques.

Dr. Addissie was selected for NRL's Jarome and Isabella Kale Distinguished Scholar Fellowship.

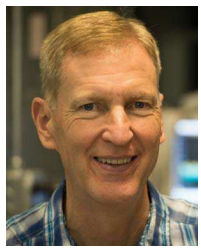

Steven M. Anlage (Member, IEEE) received the B.S. degree in physics from the Rensselaer Polytechnic Institute, Troy, NY, USA, in 1982, and the M.S. and Ph.D. degrees in applied physics from the California Institute of Technology, Pasadena, CA, USA, in 1984 and 1988, respectively.

He is currently a Professor of Physics and Faculty Affiliate with the Departments of Electrical and Computer Engineering and Materials Science and Engineering, University of Maryland, College Park, MD, USA. His graduate work concerned the physics and materials properties of quasicrystals. His postdoctoral work with the Beasley–Geballe–Kapitulnik group, Stanford University, Stanford, CA, USA, from 1987 to 1990, concentrated on high-frequency properties of high temperature superconductors, including both basic physics and applications to tunable microwave devices. In 1990, he was appointed as an Assistant Professor of Physics with the Center for Superconductivity Research, University of Maryland, then Associate Professor, in 1997, and finally Full Professor of Physics, in 2002. He was the interim Director of the Center for Nanophysics and Advanced Materials, from 2007 to 2009, and is a Member of the Maryland NanoCenter. He is currently part of the Quantum Materials Center with the Department of Physics. In 2011, he was appointed as a Visiting Professor with the Center for Functional Nanostructures, Karlsruhe Institute of Technology, Karlsruhe, Germany, and in 2019, was a Visiting Fellow with the Institute of Advanced Studies, Loughborough University, Loughborough, U.K. He has coauthored more than 200 research papers in scientific journals. His research on wave propagation in complex enclosures has focused on experimental tests of the Random Coupling Model and its extensions to include short-orbits, radiation efficiency, and generalization to nonlinear systems in the time-domain. Recent work includes the use of complex enclosures as a physical realization of a reservoir computer for use in real-time processing of high-speed signals, including prediction of chaotic time-domain waveforms as an observer task.

Dr. Anlage is a Member of the American Physical Society and the Materials Research Society.

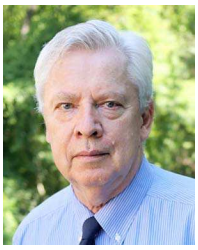

Thomas Antonsen (Fellow, IEEE) received the bachelor's, master's, and Ph.D. degrees in electrical engineering from Cornell University, in 1973, 1976, and 1977, respectively.

He was a National Research Council Post Doctoral Fellow with the Naval Research Laboratory, Washington, DC, USA, from 1976 to 1977, and a Research Scientist with the Research Laboratory of Electronics, Massachusetts Institute of Technology, Cambridge, MA, USA, from 1977 to 1980. In 1980, he moved to the University of Maryland, College Park, MD, USA, where he joined the faculty of the departments of Electrical Engineering and Physics, in 1984. He is currently a Distinguished University Professor, Professor of Physics, and the Electrical and Computer Engineering Professor of Electrophysics. He has held visiting appointments with the Institute for Theoretical Physics (U.C.S.B.), the Ecole Polytechnique Federale de Lausanne, Lausanne, Switzerland, the University of Nottingham, Nottingham, U.K., and the Institute de Physique Theorique, Ecole Polytechnique, Palaiseau, France. He served as the acting Director of the Institute for Plasma Research, University of Maryland, from 1998 to 2000. In 2017, he was elevated to the position of Distinguished University Professor. He is the author and coauthor of over 450 journal articles and coauthor of the book *Principles of Free-electron Lasers* (Springer). His research interests include the theory of magnetically confined plasmas, the theory and design of high power sources of coherent radiation, nonlinear dynamics in fluids, and the theory of the interaction of intense laser pulses and plasmas.

Prof. Antonsen was selected as a Fellow of the Division of Plasma Physics of the American Physical Society, in 1986. He was the corecipient of the Robert L. Woods award for Excellence in Vacuum Electronics Technology, and the recipient of the 2003 IEEE Plasma Science and Applications Award, the Outstanding Faculty Research Award of the Clark School of Engineering, in 2004, the IEEE J. R. Pierce Award for contributions to vacuum electronics, in 2016, and the 2022 IEEE Marie Sklodowska-Curie Award. In 2010, he served as Chair of the Division of Plasma Physics of the American Physical Society. He has served on the editorial board of *Physical Review Letters*, *The Physics of Fluids*, and *Comments on Plasma Physics*.

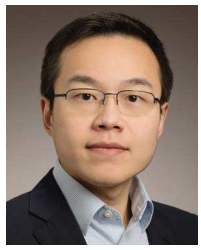

Zhen Peng (Senior Member, IEEE) received the B.S. degree in electrical engineering and information science from the University of Science and Technology of China, Hefei, China, in 2003, and the Ph.D. degree in electromagnetics and microwave engineering from the Chinese Academy of Science, Beijing, China, in 2008.

From 2008 to 2013, he was with the ElectroScience Laboratory, The Ohio State University, Columbus, OH, USA, first as a Postdoctoral Fellow, from 2008 to 2009, and then as a Senior Research Associate, from 2010 to 2013. From 2013 to 2019, he was an Assistant Professor with the Department of Electrical and Computer Engineering, The University of New Mexico, Albuquerque, NM, USA. He is currently an Associate Professor with the Department of Electrical and Computer Engineering (ECE ILLINOIS), University of Illinois at Urbana-Champaign, Champaign, IL, USA. His research interests inlcude computational, statistical and applied electromagnetics. The goal is to simulate classical and quantum electrodynamic physics with intelligent algorithms on state-of-the-art computers, where virtual experiments can be performed for the prediction, discovery, and design of complex systems at unprecedented scales. His research work has an impact on both civilian and commercial engineering applications, including advanced antennas, radio frequency integrated circuits, electromagnetic interference and compatibility, signal and power integrity, and wireless communication.

Dr. Peng was the recipient of the 2022 Best Electromagnetics Paper Award at the 16th European Conference on Antennas and Propagation, 2021 Best Paper Award at 30th Conference on Electrical Performance of Electronic Packaging and Systems (EPEPS), 2019 Best Paper Award at IEEE Electromagnetic Compatibility (EMC) Symposium, 2018 National Science Foundation CAREER Award, 2018 Best Transaction Paper Award—IEEE Transactions on Components, Packaging and Manufacturing Technology, 2017 IEEE Albuquerque Section Outstanding Young Engineer Award, 2016 UNM Electrical and Computer Engineering Department's Distinguished Researcher Award, 2015 Applied Computational Electromagnetics Society (ACES) Early Career Award, 2014 IEEE Antenna and Propagation Sergei A. Schelkunoff Transactions Prize Paper Award, a number of Young Scientist Awards, and the advisor of Best Student Paper Awards from various conferences.